Naturalis Repository

Earliest hominin occupation of Sulawesi, Indonesia

Gerrit D. van den Bergh, Bo Li, Adam Brumm, Rainer Grün, Dida Yurnaldi, Mark W. Moore, Iwan Kurniawan, Ruly Setiawan, Fachroel Aziz, Richard G. Roberts, Suyono, Michael Storey, Erick Setiabudi & Michael J. Morwood

Downloaded from
https://doi.org/10.1038/nature16448

Article 25fa Dutch Copyright Act (DCA) - End User Rights

This publication is distributed under the terms of Article 25fa of the Dutch Copyright Act (Auteurswet) with consent from the author. Dutch law entitles the maker of a short scientific work funded either wholly or partially by Dutch public funds to make that work publicly available following a reasonable period after the work was first published, provided that reference is made to the source of the first publication of the work.

This publication is distributed under the Naturalis Biodiversity Center 'Taverne implementation' programme. In this programme, research output of Naturalis researchers and collection managers that complies with the legal requirements of Article 25fa of the Dutch Copyright Act is distributed online and free of barriers in the Naturalis institutional repository. Research output is distributed six months after its first online publication in the original published version and with proper attribution to the source of the original publication.

You are permitted to download and use the publication for personal purposes. All rights remain with the author(s) and copyrights owner(s) of this work. Any use of the publication other than authorized under this license or copyright law is prohibited.

If you believe that digital publication of certain material infringes any of your rights or (privacy) interests, please let the department of Collection Information know, stating your reasons. In case of a legitimate complaint, Collection Information will make the material inaccessible. Please contact us through email: collectie.informatie@naturalis.nl. We will contact you as soon as possible.

LETTER

doi:10.1038/nature16448

Earliest hominin occupation of Sulawesi, Indonesia

Gerrit D. van den Bergh[1,2], Bo Li[1], Adam Brumm[3,4], Rainer Grün[3], Dida Yurnaldi[1,5], Mark W. Moore[6], Iwan Kurniawan[5], Ruly Setiawan[1,5], Fachroel Aziz[5], Richard G. Roberts[1], Suyono[5], Michael Storey[7], Erick Setiabudi[5] & Michael J. Morwood[1]‡

Sulawesi is the largest and oldest island within Wallacea, a vast zone of oceanic islands separating continental Asia from the Pleistocene landmass of Australia and Papua (Sahul). By one million years ago an unknown hominin lineage had colonized Flores immediately to the south[1], and by about 50 thousand years ago, modern humans (*Homo sapiens*) had crossed to Sahul[2,3]. On the basis of position, oceanic currents and biogeographical context, Sulawesi probably played a pivotal part in these dispersals[4]. Uranium-series dating of speleothem deposits associated with rock art in the limestone karst region of Maros in southwest Sulawesi has revealed that humans were living on the island at least 40 thousand years ago (ref. 5). Here we report new excavations at Talepu in the Walanae Basin northeast of Maros, where *in situ* stone artefacts associated with fossil remains of megafauna (*Bubalus* sp., *Stegodon* and *Celebochoerus*) have been recovered from stratified deposits that accumulated from before 200 thousand years ago until about 100 thousand years ago. Our findings suggest that Sulawesi, like Flores, was host to a long-established population of archaic hominins, the ancestral origins and taxonomic status of which remain elusive.

In the late 1940s the discovery of ‘Palaeolithic’ stone artefacts in association with Pleistocene fossil fauna in the Walanae Basin of south Sulawesi[6] (Fig. 1) led to considerable speculation about the time depth of human occupation of the island[7,8]. The lithic assemblages comprised cores, choppers and flakes (the ‘Cabenge Industry’), and derived from undated surface collections along the eastern side of the Walanae River[6–8], which follows the Walanae Depression, an elongated north–south-trending fault-bounded basin (Extended Data Fig. 1). Fossils of several now-extinct species, including two pygmy proboscideans, a giant tortoise and a large endemic suid, *Celebochoerus*, were recovered from the same unstratified contexts[9,10] and excavations at various sites[11]. Despite protracted investigations, the stratigraphic context and time range of the ‘Cabenge Industry’ remained unresolved because of a lack of *in situ* stone artefacts[11].

To clarify these issues we conducted surveys in the Cabenge area between 2007 and 2012, leading to the discovery of four new sites with *in situ* stone artefacts in their stratigraphic context. At Talepu, one of the newly discovered sites, we undertook deep-trench excavations. The site is 3 km southeast of Cabenge and 13 km downstream from where the Walanae River leaves its confining valley and enters a widening, actively subsiding floodplain towards the north (Extended Data Fig. 1). During the Pleistocene, east–west compression and wrench faulting along the Walanae fault zone resulted in uplift of the Sengkang anticline and the southern part of the Walanae Depression[12,13]. In these uplifted areas the folded Pliocene–Pleistocene sedimentary sequences of the Walanae Formation are now exposed[11]. In the northern part of the Walanae Depression, compressional down-folding facilitated accumulation of fluvio-lacustrine sediments from the Pleistocene to recent times. The Talepu site (4° 22′ 06.5′′ S, 119° 59′ 01.7′′ E) is near the hinge line between the uplifted southern part and the subsiding northern part of the Walanae Depression.

Our excavations focused on the northernmost hill of an elongated ridge near Talepu village, ∼600 m west of the Walanae River (Extended Data Fig. 1d). The Talepu Hill summit lies 32 m above sea level and 18 m above the adjacent Walanae River floodplain. Deposits exposed along this ridge comprise a coarsening-upward sequence of sub-horizontal fluvio-estuarine sand and silt layers overlain by alluvial cobble gravels (Extended Data Fig. 2). Two deep excavations were undertaken at Talepu (trenches T2 and T4) to provide a combined 18.7 m long stratigraphic section exposing five main sedimentary units: units A–E in descending order of depth (Fig. 2).

These excavations revealed the first evidence of *in situ* stone artefacts in securely stratified and dated contexts within the Walanae Basin. The T2 excavation yielded 270 stone artefacts between the surface and 4.2 m depth (Fig. 3a–i, Extended Data Fig. 3b and Supplementary Table 1) which are associated with unit A’s high-energy fluvial gravel deposits. Hence most are water-rolled to various degrees, although 21% are in relatively fresh condition. The main source of raw material is coarse- to medium-grained silicified limestone cobbles measuring up to 130 mm in diameter. Most are medium- to large-sized flakes (Supplementary Table 2), with cores comprising 13% of the assemblage. Cores were reduced by hard-hammer blows to one face (42%) or bifacially (58%) from unprepared striking platforms. Core reduction was not intensive although seven cobbles were rotated and subsequent reduction created multiplatform cores. Flakes struck from the cobbles were themselves reduced to one face (60%) or bifacially (40%). Although there is patterning in the flaking techniques, there is little evidence that the stoneworkers were creating tools of specific form; rather, stone-flaking produced sharp-edged flakes for use or as a source for additional flakes.

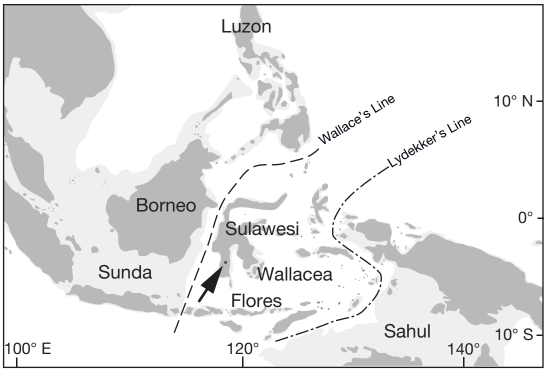

Figure 1 | Sunda, Sahul and Wallacea. Wallacea has two major biogeographical boundaries: Wallace’s Line to the west and Lydekker’s Line to the east. Exposed land during periods of low sea level (−120 m) is lightly shaded. Talepu Area indicated by an arrow.

---

[1]Centre for Archaeological Science, School of Earth & Environmental Sciences, University of Wollongong, Wollongong, New South Wales 2522, Australia. [2]Naturalis Biodiversity Center, 2333 CR Leiden, The Netherlands. [3]Research Centre for Human Evolution, Environmental Futures Research Institute, Griffith University, Nathan, Queensland 4111, Australia. [4]School of Earth and Environmental Sciences, University of Wollongong, Wollongong, New South Wales 2522, Australia. [5]Geology Museum Bandung, Geological Agency, Jalan Diponegoro 57, Bandung 40122, Indonesia. [6]Archaeology, School of Humanities, University of New England, Armidale, New South Wales 2350, Australia. [7]Quadlab, Natural History Museum of Denmark, University of Copenhagen, Øster Voldgade 5-7, 13 DK-1350 Copenhagen, Denmark.
‡Deceased.

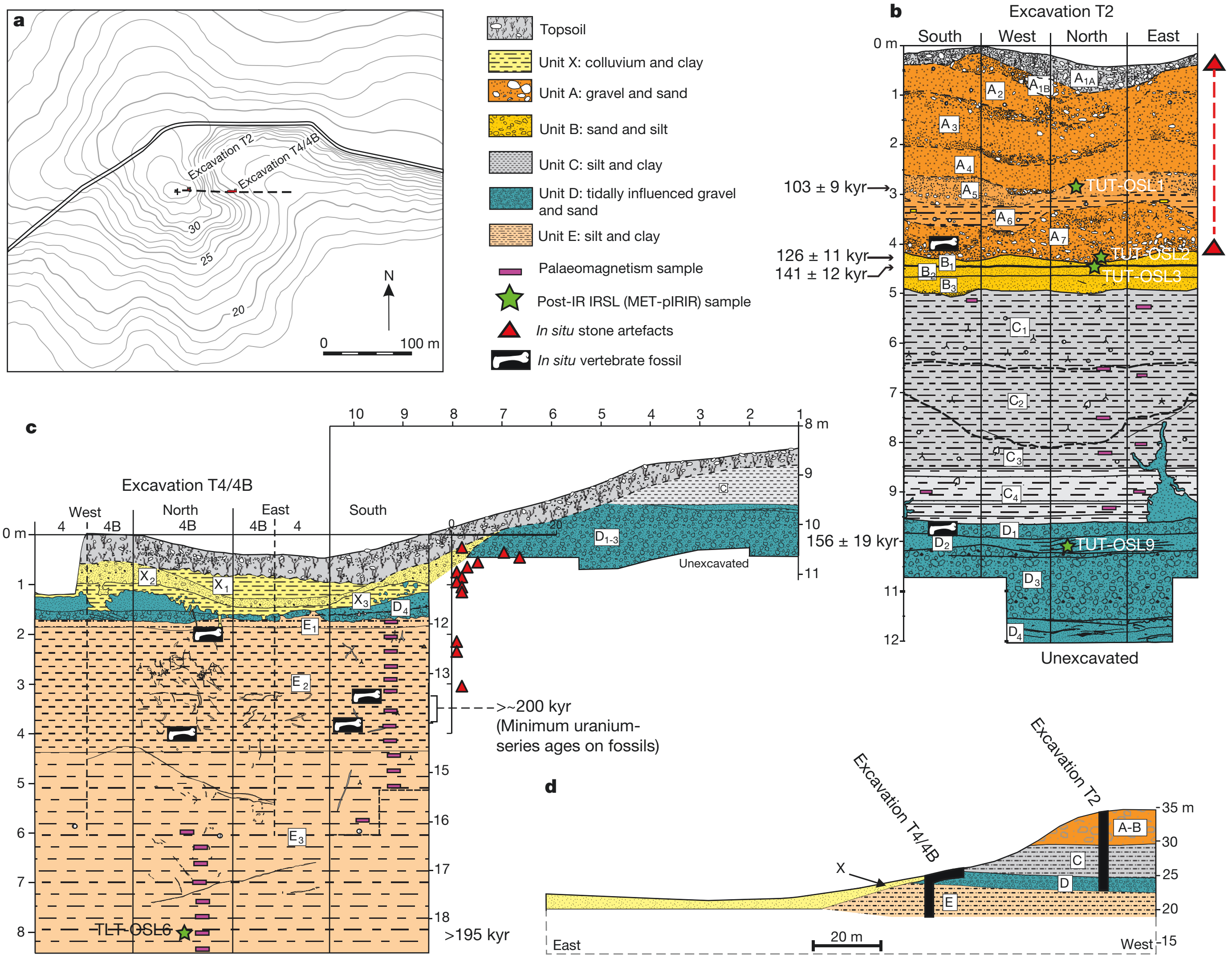

Figure 2 | Talepu excavations T2 and T4. a, Site map showing positions of T2 and T4. Dotted line indicates profile shown in **d**; stratigraphy, fossil and stone artefact occurrences, dating sampling horizons and ages for excavations T2 (**b**) and T4 (**c**). Layer key: unit A, conglomerate interval with seven distinct layers: A_1, black topsoil; A_2, sandy pebbly clay; A_3, pebbly sand; A_4 and A_5, coarse pebbly sand; A_6, silty clay; A_7, gravel; unit B, sandy unit: B_1, well-sorted, laminated silty sand; B_2, medium- to fine-grained sand; B_3, well-sorted sand with pebbles near erosive base; unit C, fine-grained sediments: C_1, mottled silty clay; C_2, silty clay; C_3, mottled silty clay, plant remains; C_4, laminated silty clay with sandy streaks (with sandy intrusion in east baulk); unit D, coarse-grained interval: D_1, well-sorted, mottled pebbly sand; D_2, very coarse cross-bedded sand with rip clasts and mud drapes; D_3, clast-supported gravel with rip clasts; D_4, medium- to fine-grained cross-bedded sand alternating with mud drapes; unit E, fine-grained sediments: E_1, clayey silt; E_2, mottled silts; E_3, clayey silts. Colluvial unit X unconformably overlies unit D. Vertical distribution of *in situ* artefacts in T4 plotted as number of artefacts per 10 cm interval.

From T4 we recovered 41 stone artefacts from the topsoil and colluvium down to a depth of 120 cm. However, four *in situ* silicified limestone artefacts were in exposed older strata within the silt of sub-unit E_2 (Fig. 2c), and provide the stratigraphically earliest evidence for human activity at Talepu. Two are unmodified flakes (2.2–2.4 m depth) (Fig. 3l–m) and two are angular scatter fragments (3.0–3.1 m depth) (Fig. 3j–k), probably created in percussion flaking. The latter are made of a distinctive mottled silicified limestone and appear to have been removed from the same core. The artefacts bear no evidence of water transport; indeed, unit E did not yield any clasts indicative of high-energy water flow.

Only one identifiable fossil was found in T2: a bovid lower molar fragment (4 m depth) (Fig. 3t) that falls just above the size range of the extant lowland anoa, *Bubalus depressicornis* (Extended Data Fig. 3e). T4 yielded eight *Celebochoerus* dental elements (for example, a lower canine; Fig. 3o) and three unidentifiable bone fragments, from the silty interval of sub-unit E_2 (between 3.1–4.0 m below the surface) and just beneath the lowest stone artefacts. At least some of these fossil remains can be ascribed to one individual (Fig. 3q). A *Stegodon* milk molar fragment (1.9–2.0 m depth) (Fig. 3r) and a dermal scute of a crocodile (3.9–4.0 m) were also recovered.

To constrain the age of the Talepu deposits, we obtained uranium-series ages for teeth and bones excavated from sub-unit E_2 using laser ablation inductively coupled plasma mass spectrometry (LA-ICP-MS) methods[14] (see Methods: uranium-series dating). Sequential laser spot analyses were undertaken on cross-sections of eight *Celebochoerus* fossils found between 0.2 and 0.5 m below the deepest stone artefacts in the same silty unit (Extended Data Fig. 4a–i). Data sets were combined for each sample and a single age estimate was calculated using the diffusion-absorption-decay model[15]. Most of the age results have infinite positive error bounds, so it was only possible to calculate minimum ages[14]. The combined uranium-series results (Supplementary Table 3) indicate that the fossil samples are older than ~200 thousand years (kyr). Palaeomagnetic samples from silty layers of units A, C and E have normal magnetic polarities at all sampled levels (Extended Data Fig. 4j

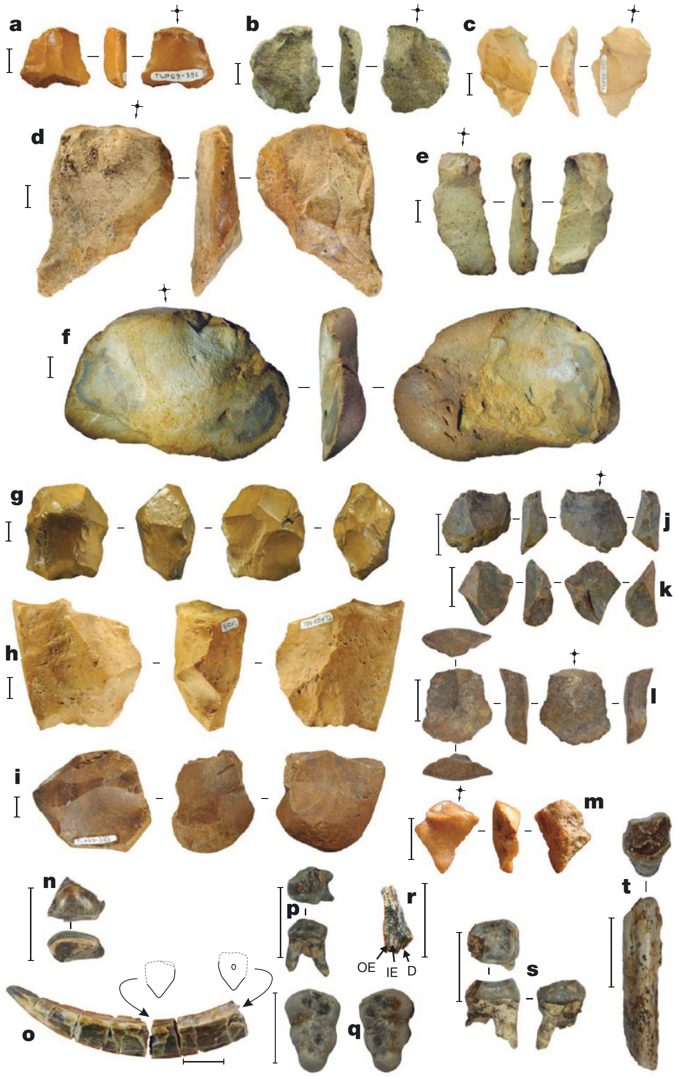

Figure 3 | Finds from Talepu excavations 2 (T2) and 4/4B (T4/T4B). All artefacts shown are silicified limestone. Flakes: **a**, T2-A$_7$, 3.7–3.8 m; **b**, T2-A$_1$, 0.4–0.5 m; **c**, T2-A$_7$, 3.6–3.7 m; **d**, T2-A$_2$, 0.9 m; **e**, T2-A$_1$, 0.2–0.3 m; **f**, T2-A$_2$, 0.8–0.9 m; **j**, T4B-E$_2$, 3.0–3.1 m; **k**, same material as **j**, but does not refit, T4B-E$_2$, 3.0–3.1 m; **l**, T4-E$_2$, 2.38 m; **m**, T4-E$_2$, 2.2–2.4 m. Cores: **g**, radial core (T2-A$_1$, 0.1–0.3 m); **h**, core (T2-A$_7$, 3.6–3.7 m); **i**, core (T2-A$_7$, 3.6–3.7 m). Fossils ('TLP' numbers refer to the Bandung Geology Museum fossil collection numbers from Talepu): **n**, upper left incisor, *Celebochoerus* sp. (TLP10-F8*, T4-E$_2$, 3.2–3.4 m); **o**, lower left canine, *Celebochoerus* sp. (TLP10-F1*, T4-E$_2$, 3.3 m); **p**, upper right third premolar, *Celebochoerus* sp. (TLP10-F5, T4-E$_2$, 3.3–3.4 m); **q**, upper right (TLP10-F3*) and upper left third molar (TLP10-F4*), *Celebochoerus* sp. (T4-E$_2$, 3.3–3.4 m); **r**, *Stegodon* molar ridge fragment (D, dentine; OE, outer enamel; IE, inner enamel; OE and IE equal thickness (TLP12-F3, T4B-E$_1$, 1.9–2 m); **s**, upper left fourth premolar, *Celebochoerus* sp. (TLP10-F2*, T4-E$_2$, 3.2–3.3 m); **t**, lower left third molar fragment, Bovidae, cf. *Bubalus* sp. (TLP09-F2, T2-A$_7$, 4–4.1 m). *Fossils used for uranium–series dating. Scale bars: **a**–**i**, 10 mm; **j**–**t**, 20 mm.

and 5). Taken together with the uranium-series results, the fossils are therefore >200 kyr and <780 kyr in age.

To constrain the age of the artefacts, a multiple-elevated-temperature post-infrared infrared stimulated luminescence (MET-pIRIR) dating procedure[16,17] was applied to potassium-rich feldspar grains extracted from five sediment samples spanning the entire sequence. The four samples analysed from T2 have ages in stratigraphic order 103 ± 9 kyr at 3 m depth to 156 ± 19 kyr at 10 m depth (Fig. 2, Methods: Optical Dating, and Supplementary Table 4). These results suggest that the Talepu cultural sequence ends at ~100 kyr, or possibly earlier (see Methods). The sediments dated to 156 ± 19 kyr were deposited near the top of unit D, which overlies the sedimentary layer (unit E) from which the deepest artefacts were excavated (more than 3 m below). The oldest securely dated evidence for stone artefacts at Talepu is, therefore, 118 kyr to 194 kyr in age at the 95% confidence interval (2σ), although human occupation of the site clearly occurred earlier given the recovery of artefacts from greater stratigraphic depths (Fig. 2c). Lastly, a sample taken at a depth of 8 m in the lower trench (T4) yielded a minimum age of ~195 kyr. This age estimate is stratigraphically consistent with the MET-pIRIR ages for T2 and with the minimum uranium-series ages of ~200 kyr for the T4 fossil remains from sub-unit E$_2$.

From our Talepu excavation results it is now possible to conclude that the initial peopling of Sulawesi took place at least 118 thousand years ago (ka). The identity of these early inhabitants is of considerable interest given previous assumptions that Sulawesi was only ever colonized by *H. sapiens*, and currently thought to have arrived in the region by ~50 ka (refs 2, 3, 18–20). The earliest *H. sapiens* skeletal remains from island Southeast Asia are ~45 kyr old[21,22]; however, modern human fossils dating to ~120 ka occur in the Levant[23], and possibly at a similar time in Southeast Asia[24]. Although controversial, it is conceivable that *H. sapiens* dispersed soon after their emergence in Africa, spread to the easternmost tip of continental Asia (Sunda) and crossed to Wallacea by ~120 ka. However, early hominins had already reached the more remote and far smaller island of Flores by 1 million years ago (ref. 1), perhaps by accidental drifting on tsunami debris[4]. It is therefore also conceivable that the first people on Sulawesi could have arrived in a similar manner at an equivalent, earlier or later time.

Our findings at Talepu attest to the presence of early tool-makers on Sulawesi by the late Middle Pleistocene, but the absence of Pleistocene human fossils on the island precludes a definitive answer as to which hominin species was first to make landfall. With regards to potential island colonizers, there are at least three candidates in the region: the known and inferred distributions of *H. floresiensis* on Flores (~190 ka (ref. 25) or earlier[1]), *H. erectus* on the southern margin of Sunda (present-day Java) (~1.5 million years ago to ~140 ka (refs 26, 27)), and 'Denisovans', whose geographic range may have extended into Wallacea[28]. Considering the predominantly southerly flowing currents of the Indonesian through-flow[29], we speculate that the most likely points of origin for the Sulawesi colonizers are Borneo to the west (part of mainland Asia during periods of low sea level) and the Philippines to the north[30] (the northern extremity of Wallacea), with the implication being that other islands in the region harbour undiscovered records of archaic hominins.

Online Content Methods, along with any additional Extended Data display items and Source Data, are available in the online version of the paper; references unique to these sections appear only in the online paper.

Received 14 April; accepted 13 November 2015.

1. Brumm, A. *et al.* Hominins on Flores, Indonesia, by one million years ago. *Nature* **464,** 748–752 (2010).
2. Clarkson, C. *et al.* The archaeology, chronology and stratigraphy of Madjedbebe (Malakunanja II): a site in northern Australia with early occupation. *J. Hum. Evol.* **83,** 46–64 (2015).
3. O'Connor, S. in *Emergence and Diversity of Modern Human Behaviour in Paleolithic Asia* (eds Yousuke Kaifu *et al.*) 214–224 (Texas A&M Univ. Press, 2015).
4. Morwood, M. & Van Oosterzee, P. *The Discovery of the Hobbit: The Scientific Breakthrough that Changed the Face of Human History* (Random House Australia, 2007).
5. Aubert, M. *et al.* Pleistocene cave art from Sulawesi, Indonesia. *Nature* **514,** 223–227 (2014).
6. Van Heekeren, H. R. Early man and fossil vertebrates on the island of Celebes. *Nature* **163,** 492 (1949).
7. Bartstra, G.-J., Keates, S. G., Basoeki & Kallupa, B. On the dispersion of *Homo sapiens* in eastern Indonesia: the Palaeolithic of south Sulawesi. *Curr. Anthropol.* **32,** 317–321 (1991).
8. van Heekeren, H. R. *The Stone Age of Indonesia* (Martinus Nijhoff, 1972).

9. Hooijer, D. A. Pleistocene vertebrates from Celebes: *Celebochoerus heekereni* nov. gen. nov. spec. *Proc. K. Ned. Akad. Wet.* **51,** 1024–1032 (1948).
10. Hooijer, D. A. Quaternary mammals west and east of Wallace's Line. *Neth. J. Zool.* **25,** 46–56 (1974).
11. van den Bergh, G. D. The Late Neogene elephantoid-bearing faunas of Indonesia and their palaeozoogeographic implications: a study of the terrestrial faunal succession of Sulawesi, Flores and Java, including evidence for early hominid dispersal east of Wallace's Line. *Scripta Geologica* **117,** 1–419 (1999).
12. Grainge, A. M. & Davies, K. G. Reef exploration in the East Sengkang Basin, Sulawesi. In *Proc. 12th Annual Convention of the Indonesian Petroleum Association*, V1, 207–227 (1983).
13. Sukamto, R. *Geological Map of Indonesia, Sheet VIII: Ujung Pandang.* Scale 1:1,000,000. Geological Research and Development Centre, Bandung (1975).
14. Grün, R., Eggins, S., Kinsley, L., Moseley, H. & Sambridge, M. Laser ablation U-series analysis of fossil bones and teeth. *Palaeogeogr. Palaeoclimatol. Palaeoecol.* **416,** 150–167 (2014).
15. Sambridge, M., Grün, R. & Eggins, S. U-series dating of bone in an open system: the diffusion-adsorption-decay model. *Quat. Geochronol.* **9,** 42–53 (2012).
16. Li, B. & Li, S.-H. Luminescence dating of K-feldspar from sediments: a protocol without anomalous fading correction. *Quat. Geochronol.* **6,** 468–479 (2011).
17. Li, B., Jacobs, Z., Roberts, R. G. & Li, S.-H. Review and assessment of the potential of post-IR IRSL dating methods to circumvent the problem of anomalous fading in feldspar luminescence. *Geochronometria* **41,** 178–201 (2014).
18. O'Connor, S., Ono, R. & Clarkson, C. Pelagic fishing at 42,000 years before the present and the maritime skills of modern humans. *Science* **334,** 1117–1121 (2011).
19. Summerhayes, G. R. *et al.* Human adaptation and plant use in highland New Guinea 49,000 to 44,000 years ago. *Science* **330,** 78–81 (2010).
20. Mellars, P. Why did modern human populations disperse from Africa *ca.* 60,000 years ago? A new model. *Proc. Natl Acad. Sci. USA* **103,** 9381–9386 (2006).
21. Storm, P. *et al.* U-series and radiocarbon analyses of human and faunal remains from Wajak, Indonesia. *J. Hum. Evol.* **64,** 356–365 (2013).
22. Barker, G. *et al.* The 'human revolution' in lowland tropical Southeast Asia: the antiquity and behavior of anatomically modern humans at Niah Cave (Sarawak, Borneo). *J. Hum. Evol.* **52,** 243–261 (2007).
23. Grün, R. *et al.* U-series and ESR analyses of bones and teeth relating to the human burials from Skhul. *J. Hum. Evol.* **49,** 316–334 (2005).
24. Westaway, K. E. *et al.* Age and biostratigraphic significance of the Punung Rainforest Fauna, East Java, Indonesia, and implications for *Pongo* and *Homo*. *J. Hum. Evol.* **53,** 709–717 (2007).
25. Westaway, K. E. *et al.* Establishing the time of initial human occupation of Liang Bua, western Flores, Indonesia. *Quat. Geochronol.* **2,** 337–343 (2007).
26. Zaim, Y. *et al.* New 1.5 million-year-old *Homo erectus* maxilla from Sangiran (Central Java, Indonesia). *J. Hum. Evol.* **61,** 363–376 (2011).
27. Indriati, E. *et al.* The age of the 20 meter Solo River terrace, Java, Indonesia and the survival of *Homo erectus* in Asia. *PLoS One* **6,** e21562 (2011).
28. Cooper, A. & Stringer, C. B. Paleontology. Did the Denisovans cross Wallace's Line? *Science* **342,** 321–323 (2013).
29. Sprintall, J. *et al.* The Indonesian seas and their role in the coupled ocean–climate system. *Nature Geosci.* **7,** 487–492 (2014).
30. Mijares, A. S. *et al.* New evidence for a 67,000-year-old human presence at Callao Cave, Luzon, Philippines. *J. Hum. Evol.* **59,** 123–132 (2010).

Supplementary Information is available in the online version of the paper.

Acknowledgements This research was supported by grants from the Australian Research Council (ARC) to M.J.M. (DP0770234/DP1093342) and G.D.v.d.B. (FT100100384), and funds from the Geological Survey Institute of Indonesia. L.B. and R.G.R. are supported by ARC Fellowships FT140100384 and FL130100116, respectively. A.B.'s involvement was supported by ARC fellowship DE130101560. The stone tool analysis was supported by ARC Fellowship DP1093342 to M.W.M., and M.S. was funded by the Villum Foundation. The fieldwork was authorized by the directors of the Geological Survey Institute of Indonesia, A. Djumarma Wirakusumah and Y. Kusumahbrata. We further acknowledge the Indonesian State Ministry of Research and Technology and the National Centre for Archaeology in Jakarta (ARKENAS), for facilitating the research. Field assistants included H. Oktaviana, Dadang, S. Sudjarwadi, Ngaliman, T. Suryana and U. P. Wibowo. During the excavations we were assisted by the landowner, Wahe, and 11 other local labourers. Y. Jafari prepared the sediment samples for optical dating and L. Kinsley assisted with the uranium-series analysis. We thank K. Westaway, D. Granger, B. Pillans and B. Jones for additional field support, and S. van der Mije for allowing access to the vertebrate collection at Naturalis. S. Hayes is thanked for providing feedback on the manuscript.

Author Contributions M.J.M. and G.D.v.d.B. conceived the study with F.A., as part of a wider project led by M.J.M., in collaboration with A.B., I.K., S. and E.S. Samples for optical dating were collected and analysed by B.L. and R.G.R. R.G. conducted the uranium-series dating and M.S. analysed samples for ^{40}Ar/^{39}Ar dating. A.B. and M.W.M. identified and analysed the stone artefacts. G.D.v.d.B. and I.K. analysed the fossil specimens. G.D.v.d.B. and R.S. recorded the site stratigraphy. D.Y. collected and analysed samples for palaeomagnetism. S. conducted a regional geological survey supervised by G.D.v.d.B. and M.J.M. G.D.v.d.B. and A.B. wrote the manuscript, with contributions from the other authors.

Author Information Reprints and permissions information is available at www.nature.com/reprints. The authors declare no competing financial interests. Readers are welcome to comment on the online version of the paper. Correspondence and requests for materials should be addressed to G.D.v.d.B. (gert@uow.edu.au) or B.L. (bli@uow.edu.au; about the optical dating method).

METHODS

Excavation methods. In 2007 and 2008 we undertook three (T1–T3) 1 m × 2 m test excavations at Talepu Hill, where large numbers of stone artefacts were found scattered on the surface with loose gravel. The summit of Talepu Hill (4° 22′ 06.5″ S; 119° 59′ 01.7″ E) lies 36 m above sea level and 18 m above the floodplain of the Walanae River, which flows 600 m to the east (Extended Data Fig. 1). Geological outcrop conditions are very poor, and thick tropical soils cover the underlying geological formations. The three test excavations near the summit of Talepu Hill proved the occurrence of *in situ* stone artefacts down to a depth of at least 1.8 m, in heavily weathered conglomerate lenses and sandy silt layers. The same gravel unit occurs on other hilltops to the west and southwest. At Bulu Palece, 850 m west of Talepu Hill, which is the highest hilltop in the vicinity with an elevation of 51 m (see Extended Data Fig. 2), the gravel is at least 13 m thick, but at Talepu Hill only a basal interval of 4.3 m thickness remains.

In October 2009, T2 was taken down to 7 m below surface (Extended Data Fig. 2b), at which depth the excavation area was reduced to a 1 m × 1 m square and taken down further to a maximum depth of 10 m. To ensure that this deep-trench operation was undertaken safely, we installed timber shoring as the work progressed (Extended Data Fig. 2c). A new east–west oriented, 1 m × 9 m trench (T4) was excavated at the base of the Talepu Hill, 40 m east of T2. This trench reached a maximum depth of 2 m, revealing the lateral development of the stratigraphy near the base of the hill (Fig. 2 and Extended Data Fig. 2d). Deposits were removed in 10 cm spits within stratigraphic units. Stone artefacts and fossils found by the excavators were bagged and labelled immediately; all other deposits were dry sieved with 5 mm mesh to separate out clasts, including stone artefacts. Pebbles from each spit were weighed; and composition analysis was undertaken on clasts from a representative sample from six spits: average maximum clast diameter was recorded by measuring the longest diameter of the ten largest clasts per spit (Extended Data Fig. 3). Bulk samples of stratigraphic units were taken for sediment and pollen analyses.

In October 2010, the excavations at Talepu were continued. A 1 m × 2 m area at the east end of T4 was excavated to a depth of 6.20 m below the surface, thus providing an additional 6 m stratigraphically below the section covered by excavation 2 in 2009. The T4 deposits were removed in 20 cm spits within stratigraphic units. After the excavation of an *in situ* stone artefact (specimen S-TLP10-1, a flake from sub-unit E_2 at a depth of 2.38 m below the surface) and fossils of *Celebochoerus*, it was decided to wet-sieve all the excavated sediments with 3 mm mesh to separate out stones and other clasts, including stone artefacts. Wet-sieving of the silty clay deposits from the interval between 2 and 2.4 m depth yielded one more stone artefact (S-TLP10-2; Fig. 3m) and two possible stone artefacts (S-TLP10-3 and S-TLP10-4). Magnetic susceptibility measurements were taken from the excavation profile at 1 cm intervals with a Bartington MS-2 device, to examine the presence of cryptic tephra layers suitable for dating. A sample for ^{40}Ar/^{39}Ar dating was taken at 2.5 m below the ground surface from an interval with elevated magnetic susceptibility values.

In October 2012, backfill of T2 and T4 was removed. T4 was enlarged with a 1 m × 2 m extension (T4-B), and both T2 and T4/4-B were taken further down with an additional 2 m and 2.1 m, respectively, to allow for sampling for palaeomagnetic and optical dating methods. In T4-B two more stone artefacts (Fig. 3j–k), originating from spit 31 (depth 3.0–3.1 m depth below ground level), were recovered on the sieves.

Stone artefacts were analysed following the definitions and methods in ref. 31. The analysis focused on stone-flaking techniques, sequences of reduction, and sizes of stone-flaking products and by-products (Supplementary Tables 1 and 2). The stone artefacts are stored at the Geology Museum in Bandung.

Uranium-series dating. The details for laser ablation uranium-series analysis of skeletal materials were recently summarized[14]. Uranium-series analyses provide insights into when uranium migrates into a bone or tooth. This may happen a short time after the burial of the skeletal element or some significant time span later. There may also be later uranium-overprints that are difficult to recognize. As such, apparent uranium-series results from faunal remains have generally to be regarded as minimum age estimates. It is very difficult or impossible to evaluate by how much the uranium-series results underestimate the correct age of the sample. Details of the instrumentation, analytical procedures and data evaluation have been modified from those described in detail elsewhere[14,32]. All isotope ratios refer to activity ratios.

Sequential laser spot analyses were undertaken on cross sections of eight *Celebochoerus* fossils from the T4 excavation at Talepu. They comprised fragments of six teeth and two bones from sub-unit E_2 found 10–50 cm below the lowest stone artefacts in the same silt layer. Of one fossil (TLP10-1, a *Celebochoerus* lower canine), two subsamples were analysed (a and b). Each fossil specimen was cut transversely using a dentist drill with a diamond saw blade (Extended Data Fig. 4). Four or five samples were then mounted together into aluminium cups, aligning the cross-sections with the outer rim of the sample holder, which later positioned the samples on the focal plane of the laser. Uranium-series isotopes were measured using the laser ablation multicollector (MC)-ICP-MS system at The Australian National University's (ANU) Research School of Earth Sciences. It consists of a Finnigan MAT Neptune MC-ICP-MS equipped with multiple Faraday cups. At the time of measurement, the mass spectrometer had only one ion counter. This necessitated two sequential sets of measurements along parallel tracks, one for ^{230}Th and a second for ^{234}U. The ion counter was set either to masses 230.1 or 234.1 while the Faraday cups measured the masses 232, 235 and 238. Samples were ablated with a Lambda Physik LPFPro ArF excimer ($\lambda = 193$ nm) laser coupled to the Neptune through an ANU-designed Helex ablation cell.

The samples were initially cleaned for 10 s with the laser spot size set to 265 μm followed by a 50 s analysis run with a 205 μm spot size using a 5 Hz pulse rate. Analyses were performed at regular intervals along traverses, all starting from the exterior surface (Extended Data Fig. 4a–i). The data sets of each transect were bracketed between reference standard analyses to correct for instrument drift.

Semi-quantitative analysis of uranium and thorium concentrations were derived from repeated measurements of the SRM NIST-610 glass (uranium = 461.5 μg g^{-1}; thorium = 457.2 μg g^{-1}), and uranium-isotope ratios from repeated measurements of rhinoceros tooth dentine from Hexian (sample 1118)[33]. Age estimates combining all measurements on a specimen were calculated using the iDAD program[15], assuming diffusion from both surfaces for the bones (TLP10-6 and 7) and roots of the teeth (Extended Data Fig. 4a–f, h, i) and directional diffusion from the central pulp cavity into the dentine and covering enamel for TLP10-9 (Extended Data Fig. 4g). The enamel data of the enamel samples were omitted as enamel has a different diffusion rate. Generally, results with elemental U/Th $<$300 are rejected, as these are associated with detrital contamination. However, this applied only to a single measurement. The finite ages are given with 2σ error bands; the infinite results only refer to the lower bound of the 2σ confidence interval (Supplementary Table 3). None of the samples showed any indication for uranium leaching, which is either expressed by sections with ^{230}Th/^{234}U $>>$ ^{234}U/^{238}U or increasing ^{230}Th/^{234}U ratios towards the surface in conjunction with decreasing uranium-concentrations.

Five samples had infinite positive error bounds and it was thus only possible to calculate minimum ages. It can be seen that the uranium-series results may change over small distances within a sample. The first data set of TLP10-1 yielded a finite result of 161 ± 15 kyr while the second set yielded a minimum age of $>$255 kyr. As mentioned above, all uranium-series results, whether they are finite of infinite, have to be regarded as minimum age estimates. If the faunal elements present a single population, the uranium-series results indicate that the Talepu samples are most probably older than $\sim$350 kyr, but certainly older than $\sim$200 kyr (Supplementary Table 3). The large errors do not allow us to further constrain the age.

Infrared stimulated luminescence dating of feldspar grains. Optical dating provides an estimate of the time since grains of quartz or potassium-rich feldspar were last exposed to sunlight[34–37]. The burial age is estimated by dividing the equivalent dose (D_e, a measure of the radiation energy absorbed by grains during their period of burial) by the environmental dose rate (the rate of supply of ionizing radiation to the grains over the same period). D_e is determined from the laboratory measurements of the optically stimulated luminescence (OSL) from quartz or the infrared stimulated luminescence (IRSL) from potassium (K)-feldspar, and the dose rate is estimated from laboratory and field measurements of the environmental radioactivity.

K-feldspar has two advantages over quartz for optical dating: (1) the IRSL signal (per unit absorbed dose) is usually much brighter than the OSL signal from quartz; and (2) the IRSL traps saturate at a much higher dose than do the OSL traps, which makes it possible to date older samples using feldspars than is feasible using the OSL signal from quartz. However, the routine dating of K-feldspars using the IRSL signal has been hampered by the malign phenomenon of 'anomalous fading' (that is, the leakage of electrons from IRSL traps at a faster rate than expected from kinetic considerations[38]), which gives rise to substantial underestimates of age unless an appropriate correction is made[39]. Recently, IRSL traps that are less prone to fading have been identified[40], using either a post-infrared IRSL (pIRIR) approach[41,42] or a MET-pIRIR procedure[16,43]. The progress, potential and remaining problems in using these pIRIR signals for dating have been reviewed recently[17].

Dating the samples from Talepu using quartz OSL is impractical because of the paucity of quartz. Furthermore, the quartz OSL traps are expected to be in saturation, owing to the ages of the samples ($>$100 kyr) and the high environmental dose rates of the deposits (4–5 Gy/kyr). In this study, we applied the MET-pIRIR procedure to K-feldspar extracts from Talepu to isolate the light-sensitive IRSL signal that is least prone to anomalous fading. We also allowed for any residual dose at the time of sediment deposition, to account for the fact that pIRIR traps are less easily bleached than the 'fast' component OSL traps in quartz. The resulting

MET-pIRIR ages should, therefore, be reliable estimates of the time of sediment deposition at Talepu.

The total environmental dose rate for K-feldspar grains consists of four components: the external gamma, beta and cosmic-ray dose rates, and the internal beta dose rate. The dosimetry data for all samples are summarized in Supplementary Table 4.

The external gamma dose rates were measured using an Exploranium GR-320 portable gamma-ray spectrometer, equipped with a 3-inch diameter NaI(Tl) crystal calibrated for uranium, thorium and potassium concentrations using the CSIRO facility at North Ryde[44]. At each sample location, three or four measurements of 300 s duration were made of the gamma dose rate at field water content. The external beta dose rate was measured by low-level beta counting using a Risø GM-25-5 multicounter system[45] and referenced to the Nussloch Loess (Nussi) standard[46]. The external beta dose rate was corrected for the effect of grain size and hydrofluoric acid etching on beta-dose attenuation. These external components of the total dose rate were adjusted for assumed long-term water contents of 20% for the Talepu Upper Trench (TUT = T2) samples and 30% for the Talepu Lower Trench (TLT = T4) sample (TUT and TLT sample numbers refer to the Centre for Archaeological Science laboratory numbers). These values are based on the measured field water contents (Supplementary Table 4), together with an assigned 1σ uncertainty of ±5% to capture the likely range of time-averaged mean values over the entire period of sample burial.

To check the equilibrium status of the ^{238}U and ^{232}Th decay chains, each sample was dried, ground to a fine powder and then analysed by high-resolution gamma-ray spectrometry (HRGS). The measured activities of ^{238}U, ^{226}Ra and ^{210}Pb in the ^{238}U series, ^{228}Ra and ^{228}Th in the ^{232}Th series, and ^{40}K are listed in Supplementary Table 5. The activities of ^{228}Ra and ^{228}Th were close to equilibrium for all of the samples, as is commonly the case with the ^{232}Th series. By contrast, the ^{238}U chain of each sample, except TUT-OSL9, was in disequilibrium at the present day. Sample TUT-OSL2 had a 39–45% deficit of ^{226}Ra and ^{210}Pb relative to the parental ^{238}U activity, whereas sample TUT-OSL3 had a 224–345% excess of the daughter nuclides. Samples TUT-OSL1 and TLT-OSL6 had ^{226}Ra deficits of 50% and 26%, respectively, relative to their ^{238}U activities, but the ^{210}Pb activities of both samples were similar to their parental ^{238}U activities.

Sample TUT-OSL3 was the only sample with a present-day excess of ^{226}Ra. This sample was from a sandy layer (unit B) through which ground water could percolate, so we attributed the observed ^{226}Ra excess to the deposition of radium transported by ground water. Given the similar ^{238}U activities of TUT-OSL3 and nearby TUT-OSL2, it is reasonable to assume that the parental uranium activity had not changed substantially during the period of burial of either sample, and that the ^{226}Ra excess in TUT-OSL3 most probably occurred recently. The latter can be deduced from the fact that ^{226}Ra has a half-life of ~1,600 years, which is short relative to the ages of our samples (>100 kyr), so any unsupported excess of ^{226}Ra would have decayed back into equilibrium with ^{238}U within ~8 kyr of deposition (that is, five half-lives of ^{226}Ra). The alternative option—that groundwater has continuously supplied excess ^{226}Ra to unit B—is not supported by the disequilibrium between ^{226}Ra and ^{210}Pb: the latter nuclide has a half-life of ~22 years, so it should remain in equilibrium with ^{226}Ra if the latter is supplied continuously and no radon gas is lost to atmosphere. Moreover, as the return of ^{210}Pb to equilibrium with ^{226}Ra is governed by the half-life of the shorter-lived nuclide, it could be argued that the excess ^{226}Ra was deposited within the past ~110 years (five half-lives of ^{210}Pb).

Fortunately, the calculated age of TUT-OSL3 is not especially sensitive to different assumptions about the timing or extent of disequilibria in the ^{238}U series. The latter accounts for only 28% of the total dose rate estimated from the HRGS data in Supplementary Table 5; this assumes that the present-day nuclide activities have prevailed throughout the period of sample burial. If, instead, as we consider more likely, the observed excess in ^{226}Ra was deposited recently and the ^{238}U decay chain had been in equilibrium for almost all of the period of sample burial, then the ^{238}U series accounted for only 12% of the total dose rate (that is, using activities of 37 ± 4 Bq kg^{-1} for ^{238}U, ^{226}Ra and ^{210}Pb). The ages calculated under these two alternative scenarios, using only the HRGS data for estimating external beta and gamma dose rates, range from ~118 kyr to ~143 kyr (Supplementary Table 5).

Sample TUT-OSL2 was from the more silty overlying layer (sub-unit A_7) and had deficits of ^{226}Ra and ^{210}Pb relative to ^{238}U, but these disequilibria were much smaller in magnitude than those of TUT-OSL3. If it were not continuously leached from the sample, ^{226}Ra will return to secular equilibrium with ^{238}U within ~8 kyr, so the existence of disequilibrium in TUT-OSL2 adds further weight to the argument for recent transport of ^{226}Ra in ground water at Talepu. The alternative is that ^{226}Ra has been leached continuously from this sample, so we performed the same sensitivity test on the dose rates and ages as that performed on TUT-OSL3. For TUT-OSL2, the ages determined using the present-day HRGS data or activities of 41 ± 3 Bq kg^{-1} for ^{238}U, ^{226}Ra and ^{210}Pb are statistically indistinguishable (130 ± 12 and 125 ± 11 kyr, respectively; Supplementary Table 5), because the disequilibria are much less marked than in TUT-OSL3 and the ^{238}U series makes only a small contribution (10–14%) to the total dose rate of TUT-OSL2.

Samples TUT-OSL1 and TLT-OSL6 had deficits of ^{226}Ra relative to ^{238}U, but similar activities of ^{238}U and ^{210}Pb. The latter additionally strengthens our proposition that ^{226}Ra was leached from these sediments recently, because ^{210}Pb should return to a state of equilibrium with ^{226}Ra within ~110 years (five half-lives of ^{210}Pb). For both samples, the ages calculated using the present-day HRGS data were statistically concordant with those estimated by assuming that the ^{238}U chain had been in secular equilibrium for almost the entire period of sample burial (Supplementary Table 5). The same applies to sample TUT-OSL9, since the measured activities of ^{238}U, ^{226}Ra and ^{210}Pb were consistent at 1σ.

To calculate the ages of the Talepu samples, we used the beta dose rates deduced from direct beta counting and the *in situ* gamma dose rates measured at each sample location. The external beta dose rates determined from beta counting and from the HRGS data (Supplementary Table 5) were statistically consistent (at 2σ) for all five samples; such agreement is expected, as both measure the present-day activities. The field gamma dose rates are also based on the nuclide activities prevailing at the time of measurement (^{214}Bi, a short-lived nuclide between ^{226}Ra and ^{210}Pb, being used for the ^{238}U series) and—importantly—take into account any spatial heterogeneity in dose rate from the ~30 cm of deposit surrounding each sample.

The *in situ* gamma dose rates for samples TUT-OSL1 and TLT-OSL6 were consistent at 1σ with those estimated from the HRGS activities, whereas the field gamma dose rates for TUT-OSL2, -OSL3 and -OSL9 were either higher or lower than those calculated from the HRGS data. The lower *in situ* gamma dose rate of TUT-OSL3 can be explained by the location of this sample close to the boundary with the TUT-OSL2 sediments, which have a smaller beta dose rate (Supplementary Table 4), and vice versa for the elevated field gamma dose rate of the latter sample. This result also indicates that the ^{226}Ra and ^{210}Pb deficits (TUT-OSL2) and excesses (TUT-OSL3) were spatially localized and not pervasive in the 30 cm of deposit surrounding these samples.

Under dim red laboratory illumination, the collected samples (see Methods) were treated with hydrochloric acid and hydrogen peroxide solutions to remove carbonates and organic matter, then dried. Grains of 90–180 or 180–212 μm in diameter were obtained by dry sieving. The K-feldspar grains were separated from quartz and heavy minerals using a sodium polytungstate solution of density 2.58 g cm^{-3}, and etched in 10% hydrofluoric acid for 40 min to clean the surfaces of the grains and remove (or greatly reduce in volume) the external alpha-irradiated layer of each grain. For each sample, 8–14 aliquots were prepared by mounting grains as a 5-mm-diameter monolayer in the centre of a 9.8-mm-diameter stainless steel disc, using 'Silkospray' silicone oil as the adhesive. This resulted in each aliquot consisting of several hundred K-feldspar grains.

The single-aliquot regenerative-dose (SAR) MET-pIRIR procedure introduced in ref. 16 was adapted for the Talepu samples in this study. We modified the original procedure by using a preheat at 320 °C (rather than 300 °C) for 60 s, to avoid significant influence from residual phosphorescence while recording the MET-pIRIR signal at 250 °C (Supplementary Table 6). In addition, following ref. 47, we used a 2 h solar simulator bleach before each regenerative dose cycle, instead of the high-temperature infrared bleaching step used originally, as this proved essential for recovering a given laboratory dose (see below).

Example IRSL (50 °C) and MET-pIRIR (100–250 °C) decay curves are shown in Extended Data Fig. 6a for an aliquot of sample TUT-OSL2. The decay curves observed at the different stimulation temperatures are similar in shape, with initial MET-pIRIR signal intensities of the order of a few thousand counts per second. Extended Data Fig. 6b shows the corresponding dose–response curves for the same aliquot. Each sensitivity-corrected (L_x/T_x) dose–response curve was fitted using a single saturating-exponential function of the form $I = I_0(1 - \exp^{-D/D_0})$, where I is the L_x/T_x value at regenerative dose D, I_0 is the saturation value of the exponential curve and D_0 is the characteristic saturation dose. The D_0 values are shown next to each dose–response curve in Extended Data Fig. 6b. For a total of 38 aliquots drawn from all 5 samples, we calculated the D_0 values for the 250 °C MET-pIRIR signal; these are plotted in Extended Data Fig. 6c. On a 'radial plot' such as this, the most precise estimates fall to the right and the least precise to the left. If these independent estimates are statistically consistent with a common value at 2σ, then 95% of the points should scatter within a band of width ±2 units projecting from the left-hand ('standardized estimate') axis to the common value on the right-hand, radial axis. The radial plot thus provides simultaneous information about the spread, precision and statistical consistency of experimental data[48–50]. The measured D_0 values range from ~220 to ~600 Gy, with the vast majority consistent at 2σ with a common value of ~360 Gy. The average D_0 value (calculated using the central age model[49]) is 358 ± 14 Gy, with the standard error taking the extent of overdispersion (16 ± 4%) into account. If we adopt the D_0 values corresponding to 90% ($2.3D_0$) and 95% ($3D_0$) of the saturation level of the typical dose–response curve as the upper limits for reliable estimation of D_e[43,47,51,37], then the maximum reliable D_e values that we can determine using the 250 °C MET-pIRIR signal are ~820 Gy and ~1070 Gy, respectively, for these samples.

To validate whether the MET-pIRIR procedure is applicable to the Talepu samples, we conducted dose recovery, anomalous fading and residual dose tests. For the latter, four aliquots of each sample were bleached for 4–5 h using a Dr Hönle solar simulator (model UVACUBE 400). The residual doses were then estimated by measuring these bleached aliquots using the modified MET-pIRIR procedure (Supplementary Table 6). The residual doses obtained for each of the TUT samples are plotted against stimulation temperature in Extended Data Fig. 7a. The IRSL signal measured at 50 °C has a few grays of residual dose, which increases as the stimulation temperature is raised, attaining values of 16–20 Gy at 250 °C. The size of the residual dose is only about 2–3% of the corresponding D_e values for the 250 °C signal, which were subtracted from the D_e values for the respective samples before calculating their ages.

It was noted in ref. 52 that a simple subtraction of the residual dose from the apparent D_e value could result in underestimation of the true D_e value if the residual signal is large relative to the bleachable signal. Accordingly, it advocated the use of an 'intensity-subtraction' procedure instead of the simple 'dose-subtraction' approach for samples with large residual doses. The dose-subtraction approach should be satisfactory for the Talepu samples, however, given the small size of the residual doses compared with the D_e values obtained from the MET-pIRIR 250 °C signal.

A dose recovery test[49] was conducted on sample TUT-OSL1. Eight aliquots were bleached by the solar simulator for 5 h, then given a 'surrogate natural' dose of 550 Gy. Four of these aliquots were measured using the original MET-pIRIR procedure[16], with a 'hot' infrared bleach of 320 °C for 100 s applied at the end of each SAR cycle (step 15 in Supplementary Table 6). The other four aliquots were measured using the modified MET-pIRIR procedure (Supplementary Table 6), with a solar simulator bleach of 2 h used at step 15. The measured doses at each stimulation temperature were then corrected for the corresponding residual doses (Extended Data Fig. 7a), and the ratios of measured dose to given dose were calculated for the IRSL and MET-pIRIR signals.

The dose recovery ratios are plotted in Extended Data Fig. 7b, which shows that a hot bleach at the end of each SAR cycle results in significant overestimation of the known (given) dose; for the MET-pIRIR 250 °C signal, an overestimation of 48% was observed. For these same four aliquots, we obtained a 'recycling ratio' (the ratio of the L_x/T_x signals for two duplicate regenerative doses) consistent with unity (1.00 ± 0.03), which indicates that the test-dose sensitivity correction worked successfully between regenerative-dose cycles. The overestimation in recovered dose, therefore, implies failure of the sensitivity correction for the surrogate natural dose: that is, the extent of sensitivity change between measurement of the surrogate natural and its corresponding test dose differs from the changes occurring in the subsequent regenerative-dose cycles. The surrogate natural and regenerative-dose cycles differ only in respect to the preceding bleaching treatment (that is, a solar simulator bleach was used for the former and a hot bleach for the latter), so we compared these results with those obtained for the four aliquots that were bleached at the end of each regenerative-dose cycle using the solar simulator. The dose recovery results improved significantly using this modified procedure (Extended Data Fig. 7): all of the measured/given dose ratios were consistent with unity (at 2σ) for the signals measured at different temperatures, with a ratio of 1.02 ± 0.03 obtained for the MET-pIRIR 250 °C signal.

The results of the dose recovery test on sample TUT-OSL1 suggest that the MET-pIRIR procedure could successfully recover a known dose given to K-feldspars from Talepu, but only when a solar simulator bleach was applied at the end of each SAR cycle. We therefore adopted this procedure to measure the D_e values for all five Talepu samples.

Previous studies of pIRIR signals have shown that the anomalous fading rate (g value) depends on the stimulation temperature, with negligible fading of MET-pIRIR signals stimulated at temperatures of 200 °C and above[16,17]. Accordingly, no fading correction is required for these high-temperature MET-pIRIR signals. To check that this finding also applied to the Talepu samples, fading tests were conducted on six aliquots of sample TUT-OSL3 that had already been used for D_e measurements. We adopted a single-aliquot procedure similar to that described in ref. 53, but based on the MET-pIRIR signals. Doses of 110 Gy were administered using the laboratory beta source, and the irradiated aliquots were then preheated and stored for periods of up to 1 week at room temperature (~20 °C). For practical reasons, we used a hot bleach (320 °C for 100 s) instead of a solar simulator bleach at the end of each SAR cycle, but this choice should not have affected the outcome of the fading test, given the aforementioned recycling ratio of unity obtained using the hot bleach. Extended Data Fig. 7c shows the decay in the sensitivity-corrected MET-pIRIR signal as a function of storage time for these six aliquots, normalized to the time of prompt measurement (which ranged from 720 s for the 50 °C IRSL to 1480 s for the 250 °C MET-pIRIR signal). The corresponding fading rates (g values) were calculated for the IRSL and MET-pIRIR signals (Extended Data Fig. 7d). The highest fading rate was observed for the 50 °C IRSL signal (5.5 ± 0.4% per decade), and decreases as the stimulation temperature is increased, falling to 0.94 ± 0.92 and 0.17 ± 1.13% per decade for the 200 and 250 °C signals, respectively. The latter g value is consistent with zero at 1σ, so we used the D_e value obtained from the 250 °C signal to date each of the samples. We note, however, that the g values for the 200 and 250 °C signals have large uncertainties, owing to the difficulty in obtaining precise estimates at low fading rates, so our data do not exclude the possibility that the high-temperature signals may fade slightly.

On the basis of the results of the performance tests described above, the MET-pIRIR procedure in Supplementary Table 6 was used to estimate the D_e values for all four TUT samples, as well as one sample (TLT-OSL6) collected from near the base of the stratigraphically underlying deposits in the TLT. The D_e estimates obtained for the TUT samples using the MET-pIRIR 250 °C signal are shown in Extended Data Fig. 8. Most of the estimates are distributed around a central value, although the spread is larger than can be explained by the measurement uncertainties alone. The overdispersion among these D_e values is ~20% for three of the TUT samples and almost twice this amount for TUT-OSL9, the latter arising from a pair of low D_e values measured with relatively high precision. To estimate the age for each of these samples, we determined the weighted mean D_e of the individual single-aliquot values using the central age model[49], which takes account of the measured overdispersion in the associated standard error.

As a further test of the reliability of our D_e estimates for the TUT samples, we have plotted the estimates of the central age model as a function of stimulation temperature in Extended Data Fig. 9a. These plots show that the D_e values increase with stimulation temperature until a 'plateau' is reached at higher temperatures for each of the TUT samples; the plateau region (marked by the dashed line) indicates that a non-fading component is present at these elevated temperatures. The existence of a plateau can be used, therefore, as an internal, diagnostic tool to confirm that a stable, non-fading component has been isolated for age determination. For all four TUT samples, a plateau is reached at temperatures of 200 °C and above, from which we infer negligible fading of the MET-pIRIR 250 °C signal. We calculated the sample ages, therefore, using the D_e values obtained from the 250 °C signal. The corresponding weighted mean D_e values, dose rate data and final ages are listed in Supplementary Table 4.

For sample TLT-OSL6 from the TLT, four of the eight aliquots measured emitted natural MET-pIRIR 250 °C signals consistent with the saturation levels of the corresponding dose–response curves (for example Extended Data Fig. 9b). This implies that the IRSL traps were saturated in the natural sample, which further supports our conclusion that the MET-pIRIR 250 °C signal had a negligible fading rate. It would be hazardous to estimate the age of sample TLT-OSL6 from the D_e values of the four non-saturated aliquots, as these may represent only the low D_e values in the 'tail' of a truncated distribution. If we adopt the average $2.3D_0$ value for the MET-pIRIR 250 °C signal of all five Talepu samples (~820 Gy) as an upper limit for reliable D_e estimation, then this corresponds to a minimum age of ~195 kyr for sample TLT-OSL6 (Supplementary Table 4).

K-feldspar chronology. The MET-pIRIR 250 °C ages for the four samples dated from the TUT (=T2) are in correct stratigraphic order, increasing from 103 ± 9 kyr (at ~3 m depth) to 156 ± 19 kyr (at ~10 m depth). They thus span the period from marine isotope stage 6—the penultimate glacial—to marine isotope stage 5, the last interglacial. This coherent sequence of ages also supports our contention that the Talepu samples were sufficiently bleached before deposition.

The sample analysed from ~8 m depth in the TLT (=T4; sample TLT-OSL6) yielded a minimum age of ~195 kyr, corresponding to marine isotope stage 7 (the penultimate interglacial) or earlier. We have not yet dated the other sediments exposed in the TLT, but expect that the 6 m of deposit immediately overlying TLT-OSL6 will be older than 156 ± 19 kyr, as they stratigraphically underlie sample TUT-OSL9 in the TUT.

We interpret the ages for the TUT samples as true (finite) depositional ages, based on the existence of D_e plateaux (Extended Data Fig. 9a) and the increase in D_e with depth (that is, ordered stratigraphically). This is the most parsimonious reading of our data. The measured fading rate of 0.17 ± 1.13% per decade for sample TUT-3 allows for the possibility, however, that the MET-pIRIR 250 °C signal may still fade slightly and that our samples had reached an equilibrium state of trap filling and emptying (so-called field saturation[54]). If so, then the increase in D_e with depth could, instead, be due to a systematic decline in fading rate with increasing depth. Any such a trend cannot be verified or rejected from laboratory measurements of the g value, owing to the size of the associated uncertainties at low fading rates (Extended Data Fig. 7c, d). The ages for the TUT samples could, therefore, be viewed conservatively as minimum ages (as for sample TLT-OSL6), given the uncertainties in the measured fading rate of the 250 °C signal and the exact level at which the signal saturates. The measured age of the uppermost sample in the sequence, TUT-OSL1, would increase by about 15% and 40% after correcting[39,55,56] for assumed fading rates of 0.5 and 1% per decade, respectively. Similarly, the measured ages of TUT-OSL2, -3 and -4 would increase by about 17, 23 and 28%, respectively, after correcting for an assumed fading rate of 0.5% per decade. Thus, whether viewed as true ages or as minimum ages, the TUT sediments were deposited more than ~100 ka.

Palaeomagnetic dating. Samples for palaeomagnetic polarity assessment were taken from the baulks of excavations Talepu 2 (T2) and Talepu 4 (T4) (Fig. 2). Samples were taken at 20–30 cm intervals using non-magnetic tools. Preferably samples in non-bioturbated silty deposits were taken. The upper conglomeratic interval of T2 was omitted because of its coarser grain size and because it appeared heavily affected by soil formation and plant root bioturbation. From each sample level, five oriented sample specimens were retrieved by carving the sediment using non-magnetic tools and fitting them into 8 cm^3 plastic cubes. The samples were labelled according to excavation, baulk and depth.

In the laboratory all specimens were treated by an alternating field demagnetizer. The mean magnetic directions for each sample are presented in Supplementary Table 7. Demagnetization was performed with intervals of 2.5–5 mT to a peak of up to 80–1,000 mT. The magnetization vectors obtained from most samples showed no more than two separated components of natural remanent magnetization (NRM) on the orthogonal planes, which means that the specimens had been affected by secondary magnetization. However, secondary magnetization was easily removed with a demagnetization of up to 5–20 mT, while the characteristic remanent magnetizations (ChRMs) could be isolated through stepwise demagnetization of up 20–40 mT, in some cases up to 50 mT. Above 40 mT most samples were completely demagnetized (Extended data Fig. 4j and Supplementary Table 8).

The mean magnetization intensities and palaeomagnetic directions are plotted against stratigraphic depth in Extended Data Fig. 5. The 90–98% intensity saturation was achieved from 1.30×10^{-4} to 3.81×10^{-3} A m^{-1} before demagnetization, and between 8.52×10^{-6} and 1.49×10^{-4} A m^{-1} after demagnetization at 20–40 mT. The direction of ChRMs is determined from the orthogonal plots in at least four or five successive measurement steps between 20 and 50 mT using principal component analysis[57] (PuffinPlot[58] and IAPD 2000 software[59]) with the maximum angular deviations setting at $<5°$. Although there are no well-defined criteria for the acceptability of palaeomagnetic data available, the $k > 30$ and $\alpha 95 < 15°$ criteria of ref. 60 were used to accept the average remanence direction for sampled levels. On the basis of these tests, all the samples ($n = 24$) throughout the Talepu sequences yielded acceptable ChRMs directions and showed a normal polarity. The ChRM directions were relatively constant throughout the sequences, except the direction of samples taken in T2 at 6.5 and 7.5 m depth, which showed steep inclinations of 56–68°. Such steep inclinations are unusual for near-equatorial regions. One possible interpretation is that post-depositional mass-movement disturbances, such as creep or a landslide, resulted in rotational movements of this interval.

The equal-area projections show that the dispersion of within-site means of the remanence directions re-group more closely together after demagnetization, and no significant change in the major remanence direction occurs with depth. The major remanent direction corresponds closely with the present magnetization direction (Extended Data Fig. 5b).

^{40}Ar/^{39}Ar fusion dating of single sanidine crystals. Sample TAL-10-01 was taken from T4, sub-unit E$_2$, at a depth of 2.5 m below the surface. Euhedral sanidine crystals up to 250 μm in length were hand-picked following standard heavy liquid and magnetic separation techniques. Crystals were loaded into wells in aluminium sample discs (diameter 18 mm) for neutron irradiation, along with the 1.185 Myr Alder Creek sanidine[61] as the neutron fluence monitor. Neutron irradiation was done in the cadmium-shielded CLICIT facility at the Oregon State University TRIGA reactor. Argon isotopic analyses of gas released by CO_2 laser fusion of single sanidine crystals (Supplementary Table 9) were made on a fully automated, high-resolution, Nu Instruments Noblesse multi-collector noble-gas mass spectrometer, using procedures documented previously[1,62]. Sample gas clean-up was through an all-metal extraction line, equipped with a −130 °C cold trap (to remove H_2O) and two water-cooled SAES GP-50 getter pumps (to absorb reactive gases). Argon isotopic analyses of unknowns, blanks and monitor minerals were performed in identical fashion. ^{40}Ar and ^{39}Ar were measured on the high-mass ion counter, ^{38}Ar and ^{37}Ar on the axial ion counter and ^{36}Ar on the low-mass ion counter, with baselines measured no less than every third cycle. Measurement of the ^{40}Ar, ^{38}Ar and ^{36}Ar ion beams was performed simultaneously, followed by sequential measurement of ^{39}Ar and ^{37}Ar. Beam switching was achieved by varying the field of the mass spectrometer magnet and with minor adjustment of the quad lenses. Data acquisition and reduction was performed using the program 'Mass Spec' (A. Deino, Berkeley Geochronology Center). Detector intercalibration and mass fractionation corrections were made using the weighted mean of a time series of measured atmospheric argon aliquots delivered from a calibrated air pipette. Decay and other constants, including correction factors for interference isotopes produced by nucleogenic reactions, are as reported in ref. 62.

The resulting age probability diagram for single sanidine crystals (Extended Data Figure 10) shows a wide range in ages with a dominant population around 9.4 million years ago (Late Miocene). This indicates that the sanidine crystals from the sample do not represent a single volcanic event, but were predominantly derived from erosion of the Miocene volcanic rocks west of the Walanae Depression and/or from Late Miocene marine sediments of the Walanae Formation.

31. Moore, M. W., Sutikna, T., Jatmiko, Morwood, M. J. & Brumm, A. Continuities in stone flaking technology at Liang Bua, Flores, Indonesia. *J. Hum. Evol.* **57,** 503–526 (2009).
32. Eggins, S. M. *et al.* In situ U-series dating by laser-ablation multi-collector ICPMS: new prospects for Quaternary geochronology. *Quat. Sci. Rev.* **24,** 2523–2538 (2005).
33. Grün, R. *et al.* ESR and U-series analyses of teeth from the palaeoanthropological site of Hexian, Anhui Province, China. *J. Hum. Evol.* **34,** 555–564 (1998).
34. Huntley, D. J., Godfrey-Smith, D. I. & Thewalt, M. L. Optical dating of sediments. *Nature* **313,** 105–107 (1985).
35. Aitken, M. J. *An Introduction to Optical Dating: The Dating of Quaternary sediments by the Use of Photon-Stimulated Luminescence* (Oxford Univ. Press, 1998).
36. Lian, O. B. & Roberts, R. G. Dating the Quaternary: progress in luminescence dating of sediments. *Quat. Sci. Rev.* **25,** 2449–2468 (2006).
37. Roberts, R. G. *et al.* Optical dating in archaeology: thirty years in retrospect and grand challenges for the future. *J. Archaeol. Sci.* **56,** 41–60 (2015).
38. Wintle, A. G. Anomalous fading of thermo-luminescence in mineral samples. *Nature* **245,** 143–144 (1973).
39. Huntley, D. J. & Lamothe, M. Ubiquity of anomalous fading in K-feldspars and the measurement and correction for it in optical dating. *Can. J. Earth Sci.* **38,** 1093–1106 (2001).
40. Thomsen, K. J., Murray, A., Jain, M. & Bøtter-Jensen, L. Laboratory fading rates of various luminescence signals from feldspar-rich sediment extracts. *Radiat. Meas.* **43,** 1474–1486 (2008).
41. Buylaert, J.-P., Murray, A., Thomsen, K. J. & Jain, M. Testing the potential of an elevated temperature IRSL signal from K-feldspar. *Radiat. Meas.* **44,** 560–565 (2009).
42. Thiel, C. *et al.* Luminescence dating of the Stratzing loess profile (Austria)—testing the potential of an elevated temperature post-IR IRSL protocol. *Quat. Int.* **234,** 23–31 (2011).
43. Li, B. & Li, S.-H. Luminescence dating of Chinese loess beyond 130 ka using the non-fading signal from K-feldspar. *Quat. Geochronol.* **10,** 24–31 (2012).
44. Hutton, J. & Prescott, J. Field and laboratory measurements of low-level thorium, uranium and potassium. *Nucl. Tracks Radiat. Meas.* **20,** 367–370 (1992).
45. Bøtter-Jensen, L. & Mejdahl, V. Assessment of beta dose-rate using a GM multi-counter system. *Nucl. Tracks Radiat. Meas.* **14,** 187–191 (1988).
46. Jacobs, Z. & Roberts, R. G. An improved single grain OSL chronology for the sedimentary deposits from Diepkloof Rockshelter, Western Cape, South Africa. *J. Archaeol. Sci.* **63,** 175–192 (2015).
47. Li, B., Roberts, R. G., Jacobs, Z. & Li, S.-H. A single-aliquot luminescence dating procedure for K-feldspar based on the dose-dependent MET-pIRIR signal sensitivity. *Quat. Geochronol.* **20,** 51–64 (2014).
48. Galbraith, R. Graphical display of estimates having differing standard errors. *Technometrics* **30,** 271–281 (1988).
49. Galbraith, R. F., Roberts, R. G., Laslett, G. M., Yoshida, H. & Olley, J. M. Optical dating of single and multiple grains of quartz from Jinmium rock shelter, northern Australia: part I, experimental design and statistical models. *Archaeometry* **41,** 339–364 (1999).
50. Galbraith, R. & Roberts, R. G. Statistical aspects of equivalent dose and error calculation and display in OSL dating: an overview and some recommendations. *Quat. Geochronol.* **11,** 1–27 (2012).
51. Li, B., Roberts, R. G., Jacobs, Z., Li, S.-H. & Guo, Y.-J. Construction of a 'global standardised growth curve'(gSGC) for infrared stimulated luminescence dating of K-feldspar. *Quat. Geochronol.* **27,** 119–130 (2015).
52. Li, B., Roberts, R. G. & Jacobs, Z. On the dose dependency of the bleachable and non-bleachable components of IRSL from K-feldspar: improved procedures for luminescence dating of Quaternary sediments. *Quat. Geochronol.* **17,** 1–13 (2013).
53. Auclair, M., Lamothe, M. & Huot, S. Measurement of anomalous fading for feldspar IRSL using SAR. *Radiat. Meas.* **37,** 487–492 (2003).
54. Huntley, D. J. & Lian, O. B. Some observations on tunnelling of trapped electrons in feldspar and their implications for optical dating. *Quat. Sci. Rev.* **25,** 2503–2512 (2006).

55. Kars, R. H., Wallinga, J. & Cohen, K. M. A new approach towards anomalous fading correction for feldspar IRSL dating—tests on samples in field saturation. *Radiat. Meas.* **43,** 786–790 (2008).
56. Li, B. & Li, S.-H. Investigations of the dose-dependent anomalous fading rate of feldspar from sediments. *J. Phys. D* **41,** 225502 (2008).
57. Kirschvink, J. L. The least-squares line and plane and the analysis of paleomagnetic data. *Geophys. J. R. Astron. Soc.* **62,** 699–718 (1980).
58. Lurcock, P. C. & Wilson, G. S. PuffinPlot: a versatile, user-friendly program for paleomagnetic analysis. *Geochem. Geophys. Geosyst.* **13,** Q06Z45 (2012).
59. Torsvik, T., Briden, J. & Smethurst, M. Super-IAPD interactive analysis of palaeomagnetic data. http://www.geodynamics.no/resources.html (2000).
60. Butler, R. F. *Paleomagnetism: Magnetic Domains to Geologic Terranes* Ch. 6, 103–120 (Blackwell Scientific, 1992).
61. Rivera, T. A., Storey, M., Schmitz, M. D. & Crowley, J. L. Age intercalibration of ^{40}Ar/^{39}Ar sanidine and chemically distinct U/Pb zircon populations from the Alder Creek Rhyolite Quaternary geochronology standard. *Chem. Geol.* **345,** 87–98 (2013).
62. Storey, M., Roberts, R. G. & Saidin, M. Astronomically calibrated ^{40}Ar/^{39}Ar age for the Toba supereruption and global synchronization of late Quaternary records. *Proc. Natl Acad. Sci. USA* **109,** 18684–18688 (2012).
63. Elburg, M. A. & Foden, J. Geochemical response to varying tectonic settings: an example from southern Sulawesi (Indonesia). *Geochim. Cosmochim. Acta* **63,** 1155–1172 (1999).
64. Wilson, M. E. J., Bosence, D. W. J. & Limbong, A. Tertiary syntectonic carbonate platform development in Indonesia. *Sedimentology* **47,** 395–419 (2000).

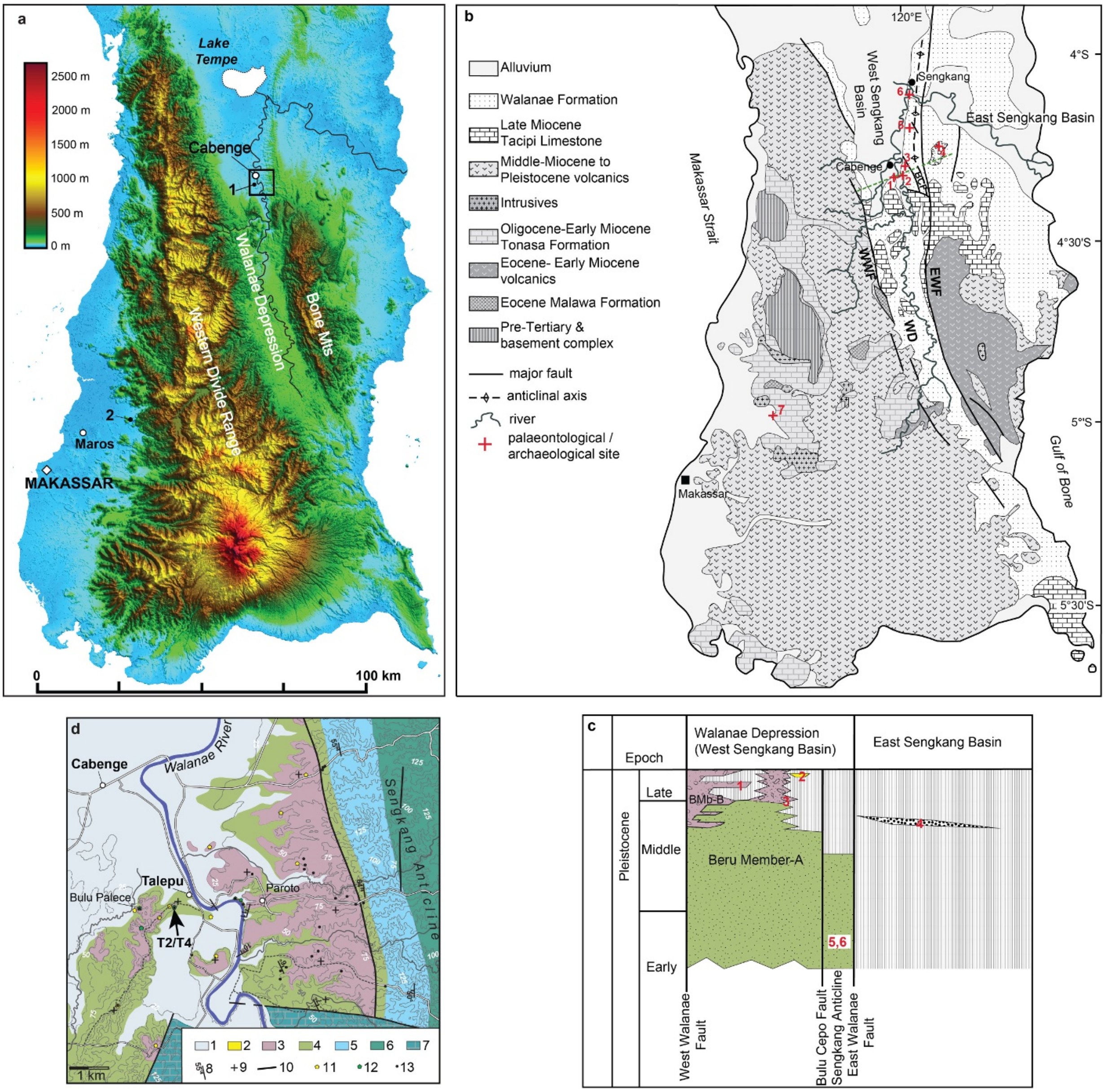

Extended Data Figure 1 | Research location and geology of southwest Sulawesi and Talepu. a, Digital elevation model of southwest Sulawesi. 1: Talepu; 2: Maros karst area. Area enclosed by rectangle shown in **d**; map data: copyright USGS/NASA SRTM (2007). **b**, Geological map of southwest Sulawesi (data from refs 11, 63, 64). The Walanae Depression (WD) is an elongate fault-bounded basin (also known as the West Sengkang Basin) separated from the Bone Mountains to the east by a major fault, the East Walanae fault (EWF), which formed in response to east–west compression and strike-slip movements along the Walanae fault zone. To the west the basin is bordered by the Western Dividing Range, consisting of uplifted Miocene volcanics deposited in a shallow marine environment[13]. The Walanae Depression basin infill consists of a several-kilometre-thick regressive sequence, named the Walanae Formation. In the southern part of the Walanae Depression, the Walanae Formation is folded and deformed by Pleistocene compression, whereas to the north near Lake Tempe deposition continues to the present day. 1: Talepu; 2: Paroto (alluvial terrace of the Walanae River); 3: Beru[8]; 4: Tanrung River (palaeontological site: coastal terrace deposits[11]); 5: Sompe[8–10]; 6: Celeko[8–10]; 7: Maros karst archaeological sites[5]. **c**, Schematic stratigraphic scheme for the northern Sengkang Basin at the latitude of the Talepu site (green dotted line in **b**). The Walanae Formation basin fill represents a regressive sequence that was strongly influenced by tectonic movements along the Walanae fault zone. The youngest unit of the Walanae Formation is the Beru member (deltaic sands, clays and gravels), which contains fossil vertebrate remains of the Walanae Fauna[11]. The lower part of the Beru member (unit A) is characterized by sedimentary structures indicative of shallow marine/estuarine/fluvial depositional environments. The upper part of the Beru member (unit B) consists of fully terrestrial fluvio-lacustrine deposits, which merge into the modern floodplain along the depocentral axis of the Walanae Depression. The coarser-grained unit B of the Beru member was not deposited in the Sengkang anticline, which started to rise during the Middle Pleistocene, or in the southern portion of the Walanae Depression south of Talepu. East of the Walanae fault Zone, in the East Sengkang Basin, uplift and folding during the Pliocene caused a depositional hiatus. Here Late Miocene deformed marine deposits of the Walanae Formation are unconformably overlaid by a conglomerate up to 5 m thick, the Tanrung Formation, which contains a distinct fossil vertebrate fauna[11]. During the Middle and Late Pleistocene, uplift of the Western Dividing Range generated the formation of alluvial fans and influxes of coarse-grained boulder conglomerates into the Walanae Depression. **d**, Geological map of Talepu area with sub-horizontal layering, fault-bounded to the east by steeply west-dipping strata of the Sengkang anticline. 1: Modern alluvium; 2: Late Pleistocene alluvial terrace; 3–7: lithological sub-units of the Walanae Formation: 3: fluvio-lacustrine facies of the upper part of the Beru member; 4: fluvio-estuarine facies of the lower part of the Beru member; 5: shallow marine facies of the Samaoling member; 6: deep marine facies of the Burecing member; 7: coral reef facies of the Tacipi member; 8: strike and dip; 9: sub-horizontal layering; 10: major fault; 11: sites with surface-collected stone artefacts; 12: sites with *in situ* stone artefacts; 13: fossil vertebrate localities.

Extended Data Figure 2 | Talepu site and excavation images. a, View to the east of the north–south trending ridge. Talepu is located behind the palm trees on the left. **b**, View towards the East Baulk of Talepu excavation 2 in 2009. In 2010 the 1 m × 2 m excavation was extended to a 2 m × 2 m excavation. **c**, The 12 m deep Talepu excavation 2 in 2012. **d**, Talepu excavation 4 in 2010. View towards the North Baulk. **e**, Talepu excavation 2 in 2012. Photograph shows the North Baulk at 4–5 m depth, with, in the upper part, the base of gravel unit A$_7$ and the three holes left by sampling for optical dating.

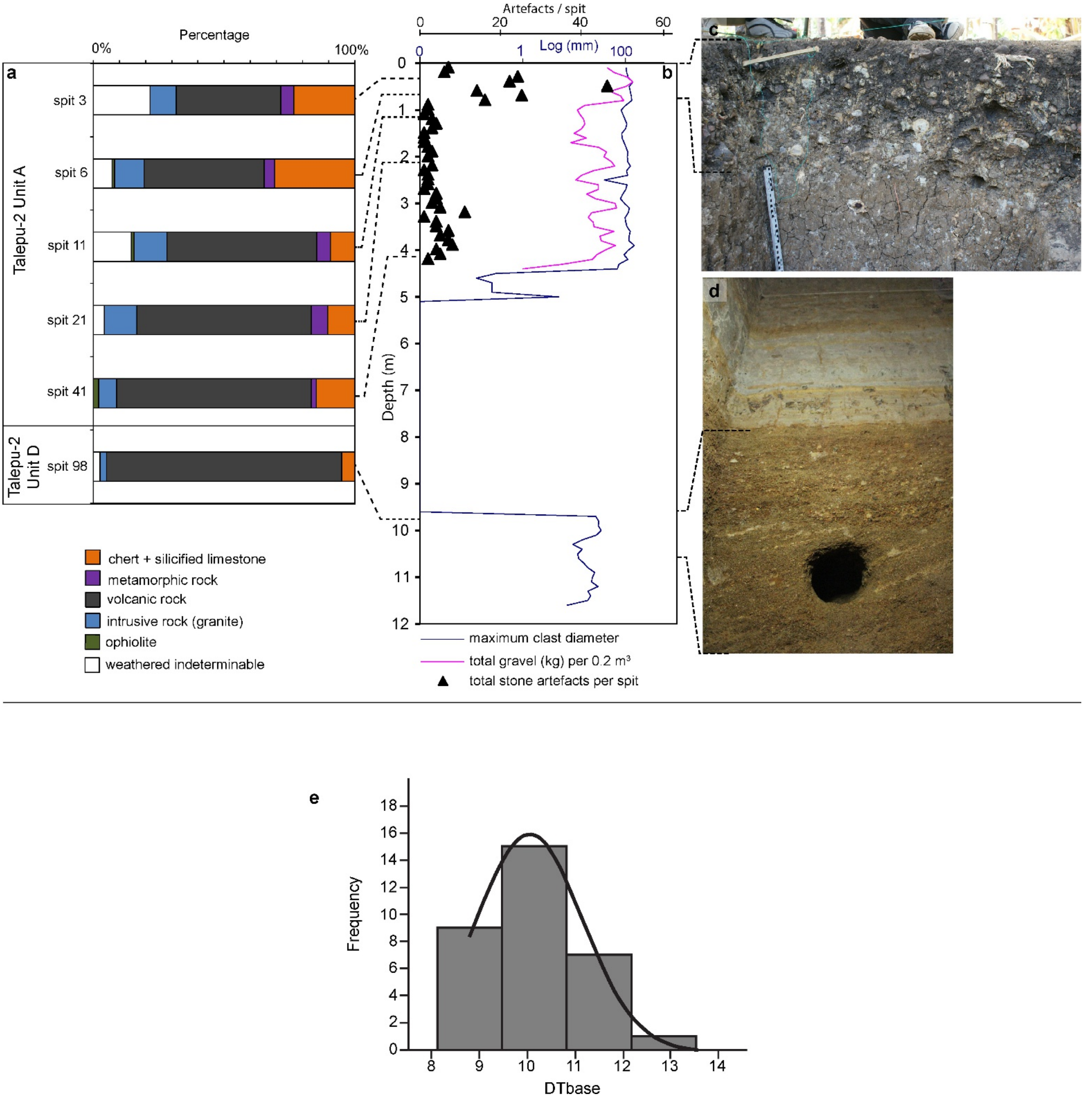

Extended Data Figure 3 | Composition of gravels and distribution of stone artefacts in T2, and size distribution of recent anoa molars. **a**, Gravel compositions based on pebble counts (200 pebbles per level). Overall, the composition of the gravel is dominated by volcanic pebbles, which become more abundant with increasing depth, probably as a result of less intense weathering further down (near the surface, the volcanic clasts are frequently weathered to a crumbly clayey 'ghost'). Note the increase both in weathering-resistant silicified rock pebbles and in heavily weathered indeterminable clasts towards the top of the sequence. **b**, Total number of artefacts per 10 cm spit (black triangles), total amount of gravel clasts per spit (red graph) and the maximum clast diameter per spit (blue graph: values represent the mean maximum clast diameter of the ten largest clasts). Note the higher concentration of both gravel and artefacts in the topsoil: pebbles and artefacts are concentrated by winnowing of sand and clay by sheetwash processes. **c**, Detail of the topsoil as exposed in the west baulk of excavation T2. **d**, Detail of the basal sequence as exposed in the north baulk of excavation T2. Note the cross-bedded foresets of the pebbly sand of sub-unit D_2, with inter-bedded mud laminae, indicative of tidal activity. Diameter of the round sample hole (for optical dating) is ~10 cm. **e**, Histogram of the transverse diameter measurements (in millimetres) of recent lowland anoa (*Bubalus* [*Anoa*] *depressicornis*) lower molars measured in the collections of the Naturalis Biodiversity Centre, Leiden, the Netherlands ($n = 32$). The lowland anoa is the largest living anoa, bigger in body size than the mountain anoa, *Bubalus* [*Anoa*] *quarlesi*. The lower molar fragment from unit A of the Talepu-2 excavation (Fig. 3t) has a preserved basal transverse diameter of 14.4 mm and an estimated basal transverse diameter of 15.5 mm, slightly above the size range for extant lowland anoa.

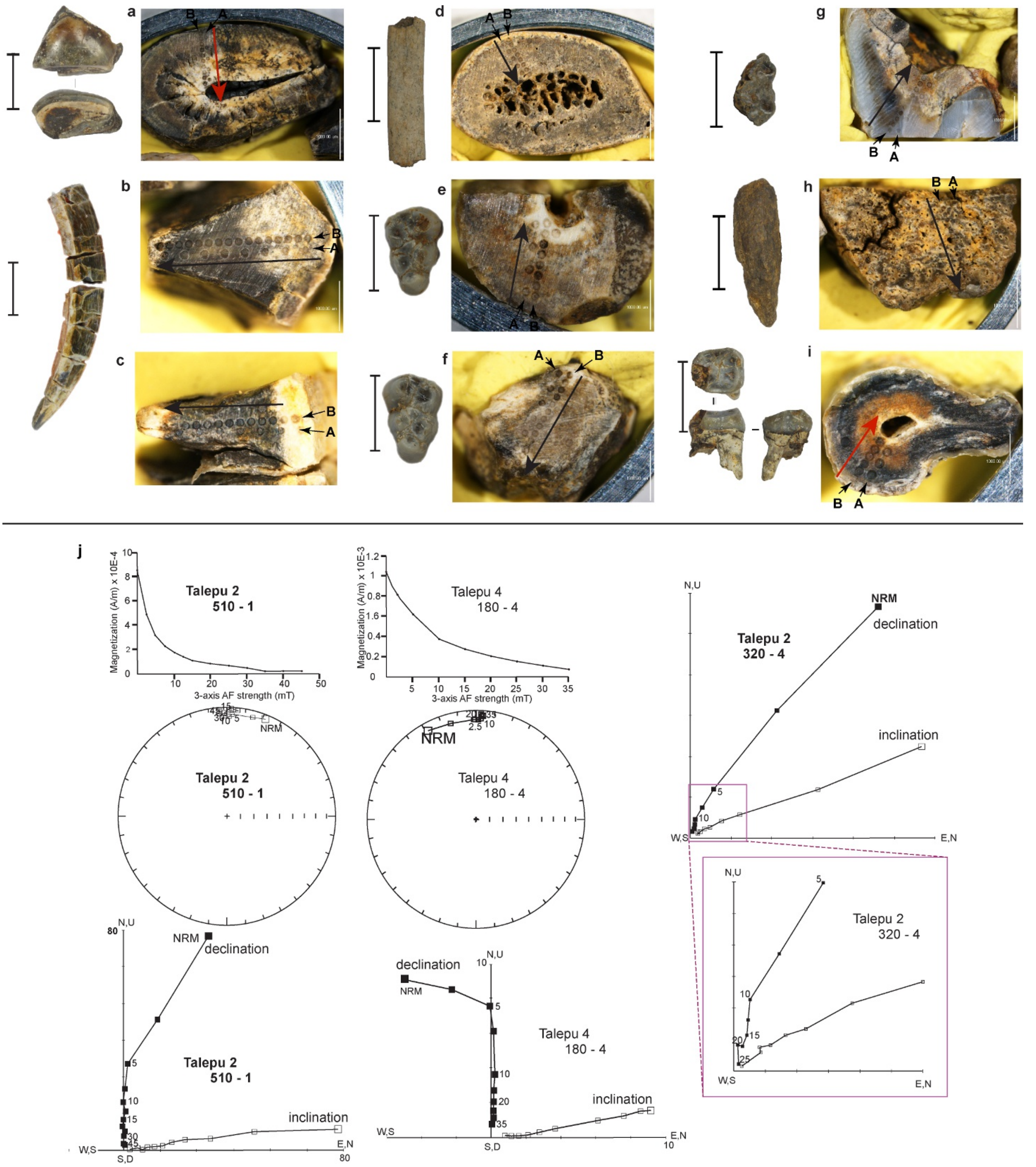

Extended Data Figure 4 | Fossil samples used for uranium-series dating and demagnetization results of representative palaeomagnetic samples. Faunal remains from Talepu excavation 4, used for uranium-series laser ablation dating (**a**–**i**) and representative NRM intensity plots of progressive demagnetization (**j**). **a**–**i**, Close-ups of the surface sections for each fossil with the laser spot profiles. All fossils originate from excavation T4, sub-unit E2. Scale bars next to fossils are 2 cm; white scale bars in close-ups are 1 mm. Numbers between brackets are Australian National University laboratory numbers. **a**, Specimen TLP10-F8 (ANU-2946), *Celebochoerus* upper left first incisor; laser ablation transect on cut section of root. **b**, **c**, Two sections measured on different transects of the same specimen, TLP10-F1 (ANU-2947 and ANU-2948), a *Celebochoerus* lower left canine. **d**, Specimen TLP10-F7 (ANU-2951), rib fragment of *Celebochoerus*; **e**, Specimen TLP10-F4 (ANU-2954), *Celebochoerus* upper left third molar; laser ablation transect on cut section of root; **f**, Specimen TLP10-F3 (ANU-2956), *Celebochoerus* upper right third molar (same individual as previous); laser ablation transect on cut section of root. **g**, Specimen TLP10-F9 (ANU-2955), *Celebochoerus* upper molar fragment; laser ablation transect on cut section of enamel and dentine. **h**, Specimen TLP10-F6 (ANU-2949), bone fragment. **i**, TLP10-F2 (ANU-2942), *Celebochoerus* upper left fourth premolar; laser ablation transect on cut section of root. **j**, NRM intensity plot of progressive demagnetization (upper left), equal area projections (middle left) and vector end-point demagnetization orthogonal plots (bottom left) for two Talepu palaeomagnetic samples (T2-510-1, T4-180-4). To the right the demagnetization curve for an additional sample (T2-320-4) is given. The inset shows the zoomed-out trajectory endpoints of sample T2-320-4. Open squares on the equal area projection diagrams indicate an upper hemisphere magnetic direction.

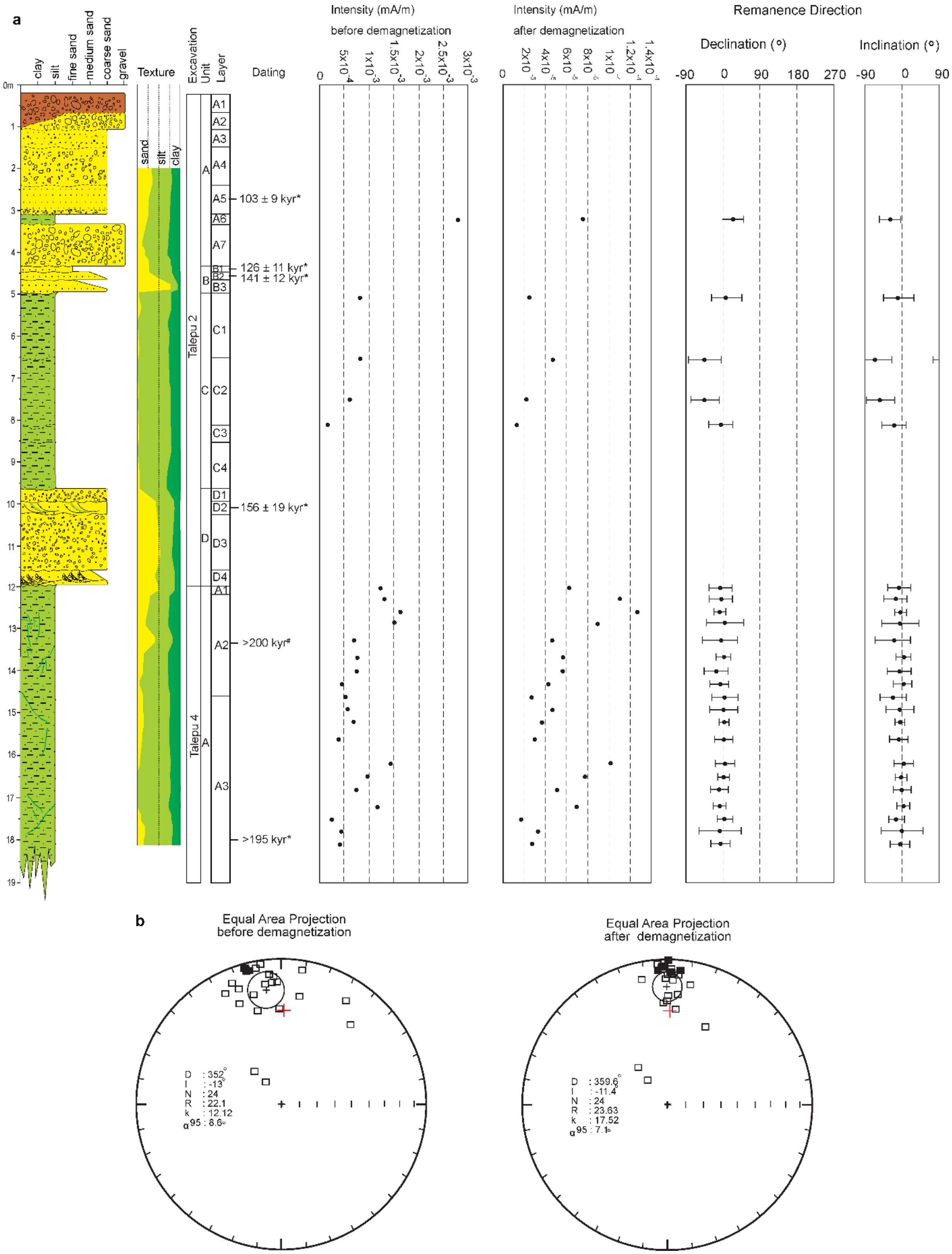

Extended Data Figure 5 | Lithological and magnetic properties against depth for the composite stratigraphic column at Talepu. a, Columns from left to right show lithology, sand/silt/clay ratios, NRM magnetic intensities before and after demagnetization, and magnetic declination and inclination directions. The intensities before and after demagnetization represent averages for each sampled level. Declination and inclination values are the averages of the higher coercivity stable magnetization (ChRM) with their 95% confidence ranges. **b**, Equal-area projections of NRM and ChRM directions for all sampled levels, and the mean direction (circles with crosses; the mean is of all sampled levels except the two levels with deviating inclinations: *n* = 22) and present-day magnetic direction in the area (red crosses).

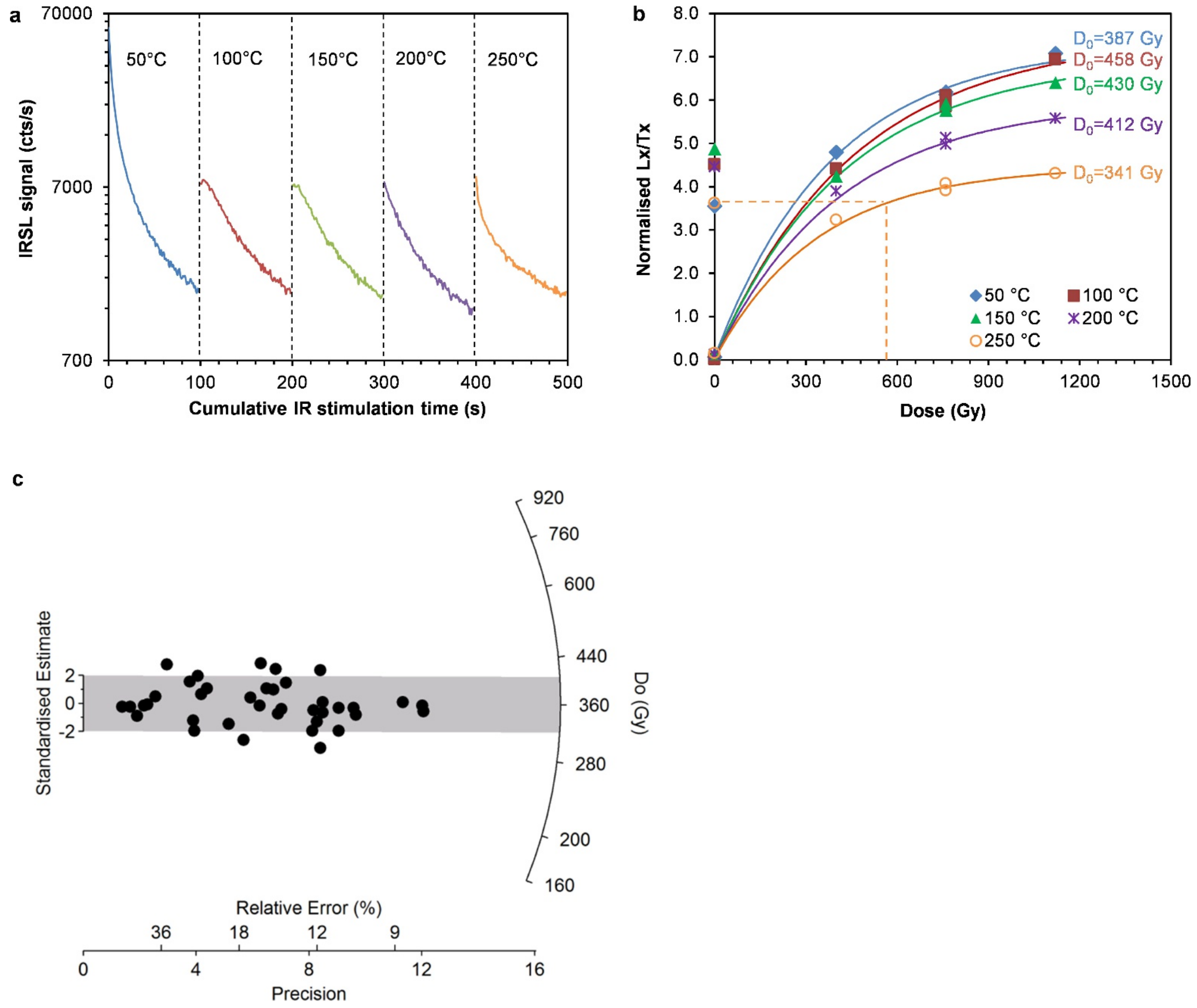

Extended Data Figure 6 | Decay curves and dose–response curves of the IRLS signals for K-feldspars from Talepu. a, Representative IRSL and MET-pIRIR decay curves for a single aliquot of sample TUT-OSL2, stimulated at different temperatures (shown above each curve). **b**, Dose–response curves for the IRSL (50 °C) and MET-pIRIR (100–250 °C) signals for the same aliquot. The natural signals are shown on the *x* axis using the same symbols as the regenerative signals. The data points were fitted using a single saturating-exponential function. The best-fit curves are shown as solid lines and the characteristic saturation dose (D_0) values are indicated. **c**, Radial plot showing the D_0 values from 38 aliquots for different samples. The grey band shows the mean of the D_0 values.

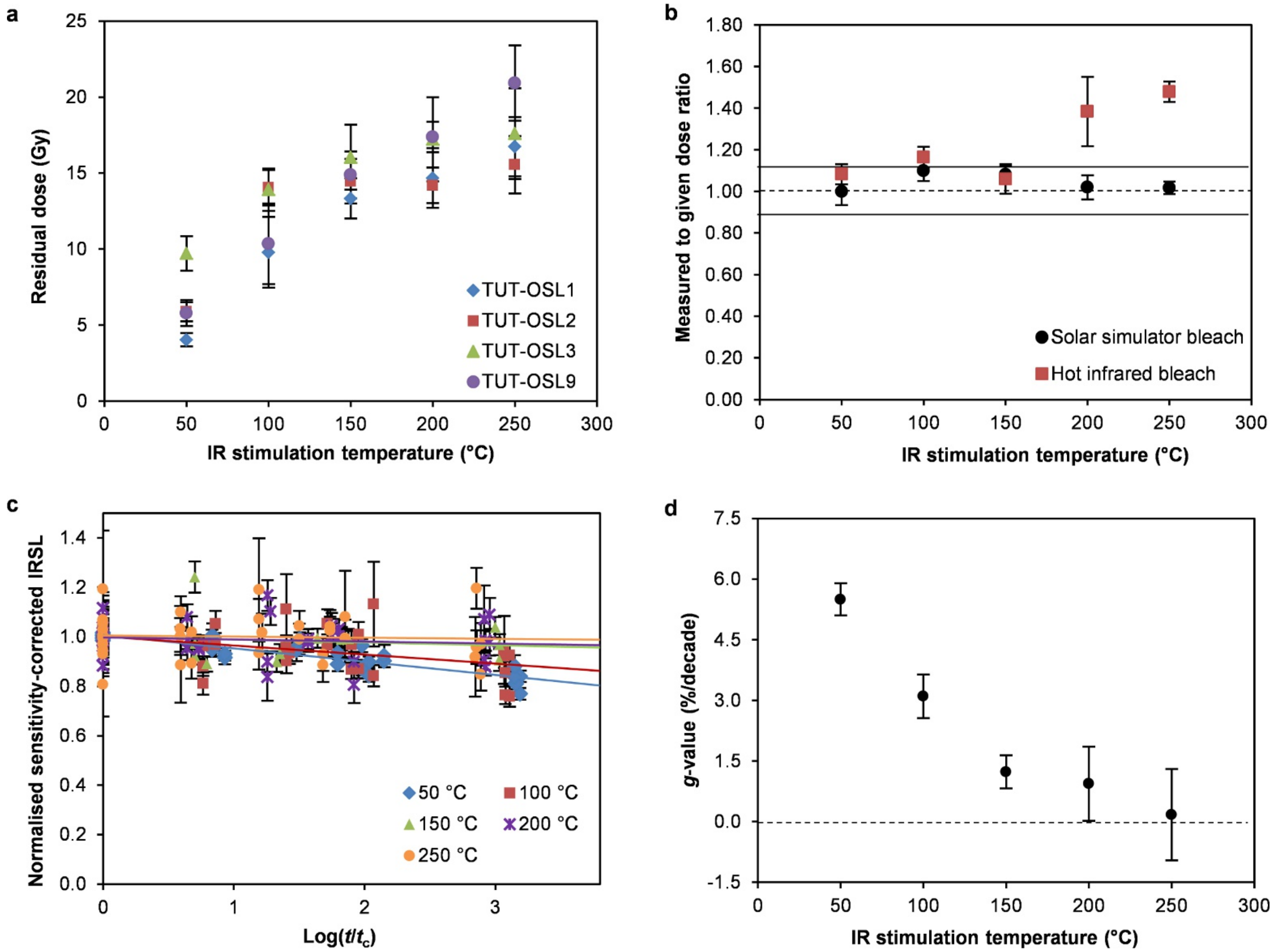

Extended Data Figure 7 | Results from residual dose, dose recovery and anomalous fading tests. a, Residual doses measured for bleached aliquots of the four samples from the upper trench, plotted against stimulation temperature. Each data point represents the mean and standard error for four aliquots. **b**, Results of the dose recovery test conducted on sample TUT-OSL1. The measured/given dose ratios are shown for the IRSL and MET-pIRIR signals at the different stimulation temperatures. Each data point represents the mean and standard error for four aliquots. The data shown in red squares were obtained using a hot IR bleach at the end of each SAR cycle, as per the conventional MET-pIRIR procedure. The data shown in black circles were obtained with the modified MET-pIRIR procedure (Supplementary Table 4), using a solar simulator bleach instead of a hot IR bleach. The dashed line denotes a ratio of unity, and the solid lines indicate ratios 10% larger and smaller than unity. The data (circles) obtained using the modified MET-pIRIR procedure fall within the latter band. **c**, Decay of the sensitivity-corrected IRSL and MET-pIRIR signals with their standard errors of six aliquots from TUT-OSL3, plotted against $\log(t/t_c)$ where t is the delayed period for each measurement and t_c is the time for the first measurement ($t_c = 720$, 870, 1,040, 1,240 and 1,480 s for the signals measured at 50, 100, 150, 200 and 250 °C, respectively). The sensitivity-corrected signals were normalized to the first measurements. **d**, Anomalous fading rates (*g* values) and their standard errors for the IRSL and MET-p IRIR signals of TUT-OSL3 obtained using the data sets in **c**, plotted against stimulation temperature. All the *g* values have been normalized to a delay time of 2 days.

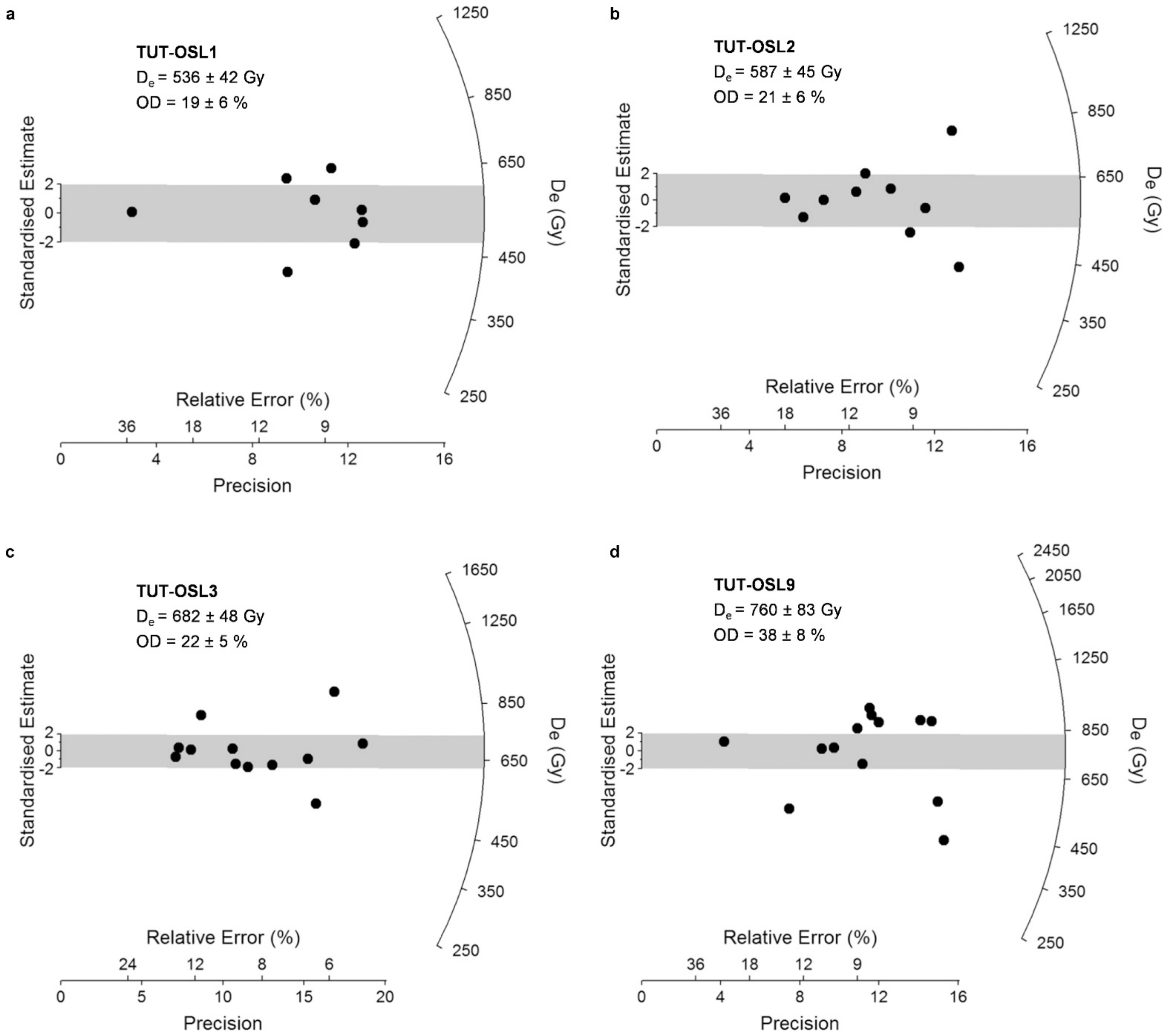

Extended Data Figure 8 | Radial plots of single-aliquot D_e values for the TUT samples. a, TUT-OSL1. **b**, TUT-OSL2. **c**, TUT-OSL3. **d**, TUT-OSL9. The grey band in each plot shows the weighted mean of the measured D_e values estimated using the central age model. The D_e estimate and the overdispersion (OD) value for each D_e distribution based on the central age model are also shown in each plot.

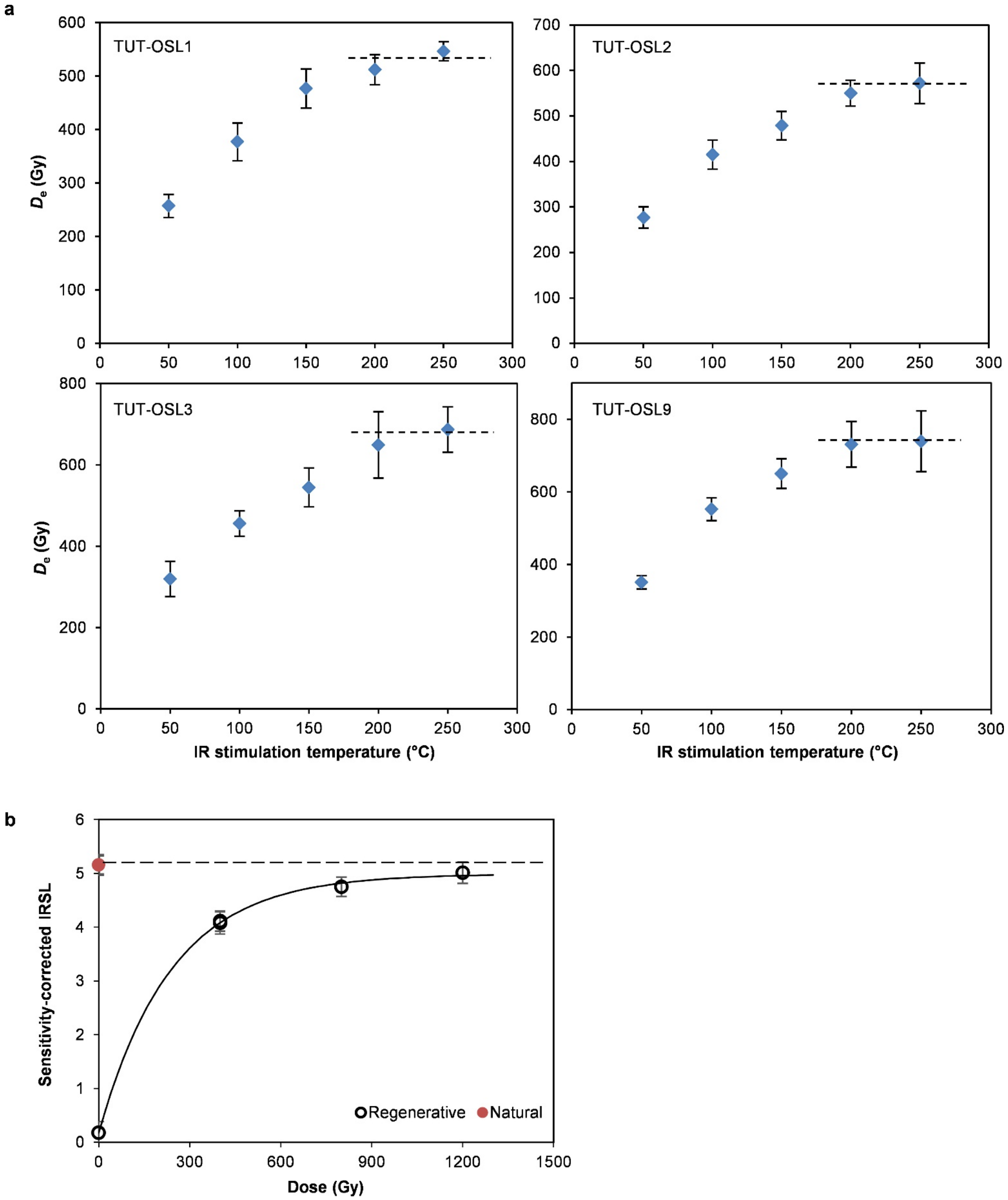

Extended Data Figure 9 | D_e versus temperature plots for the TUT samples and the dose–response curve for sample TLT-OSL6. a, Plots of the weighted mean D_e against stimulation temperature for the TUT samples. The dashed line in each plot shows the plateau range of D_e values. Each data point represents the mean and standard error for 8 (TUT-OSL1), 10 (TUT-OSL2), 12 (TUT-OSL3) and 13 (TUT-OSL9) aliquots. **b**, Dose–response curve for the sensitivity-corrected MET-pIRIR 250 °C signal from an aliquot of sample TLT-OSL6. The regenerative-dose data points and their standard errors were fitted using a single saturating-exponential function, and the best-fit curve is shown as a full line. The natural signal of this aliquot (red circle on the *y* axis) falls in the saturated region of the curve (see dashed line), so only a minimum D_e can be estimated.

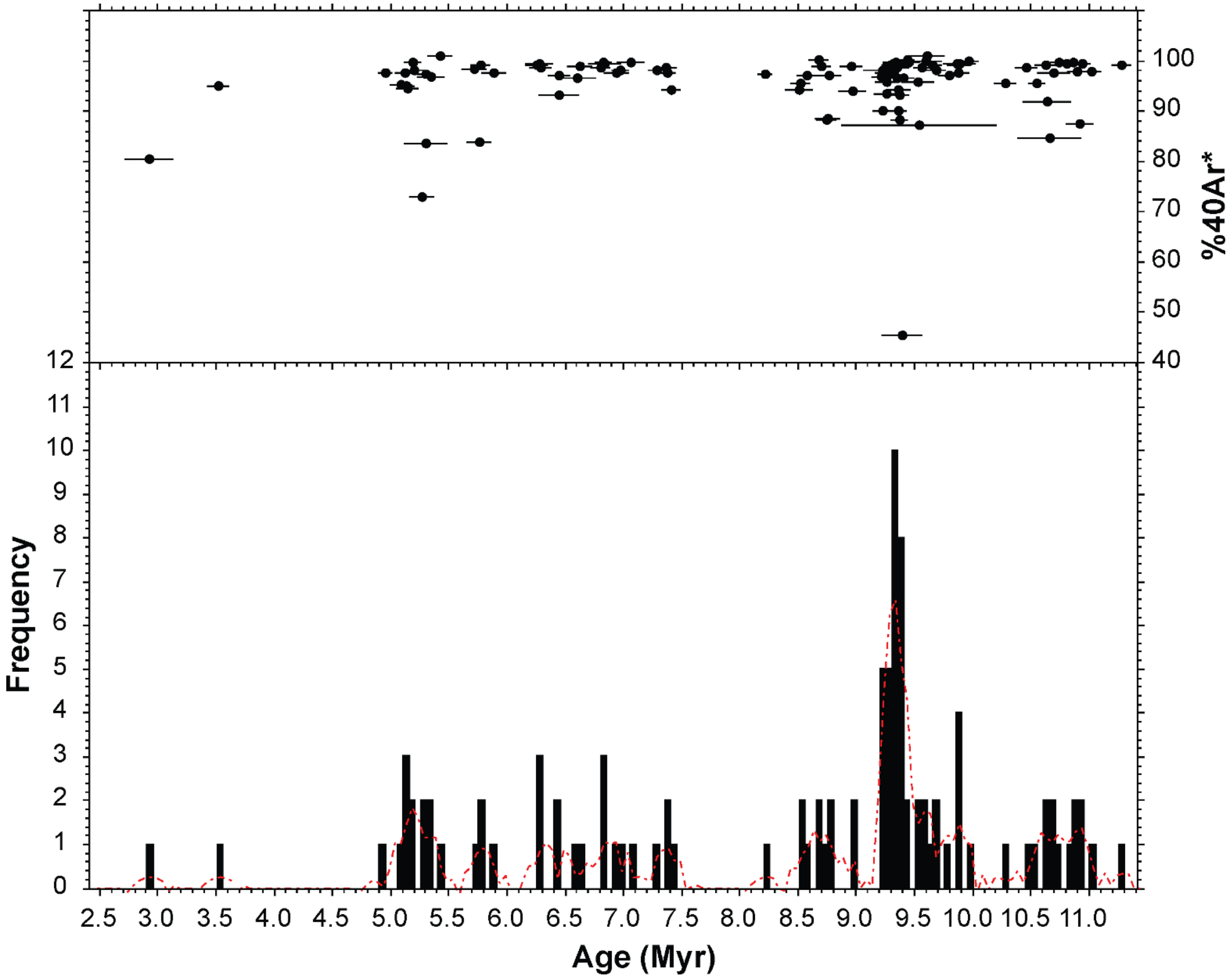

Extended Data Figure 10 | ^{40}Ar/^{39}Ar fusion ages of single sanidine crystals from sample TAL-10-01 (T4, sub-unit E$_2$, 2.5 m below surface). Top: the individual ages ± 1σ. Bottom: histogram based on over 100 analyses. Excluding the two youngest ages, the crystal ages span a period from 5 to 11 million years ago, but with the main age population at about 9.4 million years ago. The ages correspond with the Late Miocene collision phase, when potassium-rich volcanics of the Camba Formation were formed along the Western Dividing Range[63].